

# The Deep Ocean's Carbon Exhaust

Haidi Chen<sup>1</sup>, F. Alexander Haumann<sup>1</sup>, Lynne D. Talley<sup>2</sup>, Kenneth S. Johnson<sup>3</sup>, and Jorge L. Sarmiento<sup>1</sup>

<sup>1</sup>Princeton University

<sup>2</sup>Scripps Institution of Oceanography

<sup>3</sup>Monterey Bay Aquarium Res. Inst.

November 24, 2022

## Abstract

The deep ocean naturally releases large amounts of old, pre-industrial carbon dioxide (CO<sub>2</sub>) to the atmosphere through upwelling in the Southern Ocean, closing the global ocean carbon cycle. This Southern Ocean CO<sub>2</sub> release is relevant to the global climate, because its changes could alter atmospheric CO<sub>2</sub> levels on long time scales and the present-day potential of the Southern Ocean to take up anthropogenic CO<sub>2</sub>. Here, based on observational data, we show that this CO<sub>2</sub> release arises from a zonal band of subsurface waters between the Subantarctic Front and wintertime sea-ice edge with a potential partial pressure of CO<sub>2</sub> exceeding current atmospheric CO<sub>2</sub> levels ([?] $\text{PCO}_2$ ) by 175  $\mu\text{atm}$ . This band of high [?] $\text{PCO}_2$  subsurface water coincides with the outcropping of the 27.8 kg m<sup>-3</sup> isoneutral density surface that marks the upwelling of Indo-Pacific Deep Water (IPDW). Vertically, the IPDW layer exhibits a distinct [?] $\text{PCO}_2$  maximum in the deep ocean, which is set by remineralization of organic carbon and originates from the northern Pacific and Indian Ocean basins. Below this IPDW layer, the carbon content increases downwards, whereas [?] $\text{PCO}_2$  decreases. Most of this vertical [?] $\text{PCO}_2$  decline results from decreasing temperatures and increasing alkalinity due to an increased fraction of calcium carbonate dissolution. These two factors limit the CO<sub>2</sub> outgassing from the high-carbon content deep waters on more southerly surface outcrops. Our results imply that the response of Southern Ocean CO<sub>2</sub> fluxes to possible future changes in upwelling are sensitive to the subsurface carbon chemistry set by the vertical remineralization and dissolution profiles.

August 10, 2021

## The Deep Ocean's Carbon Exhaust

Haidi Chen<sup>1</sup>, F. Alexander Haumann<sup>1\*</sup>, Lynne D. Talley<sup>3</sup>, Kenneth S. Johnson<sup>4</sup>, and Jorge L. Sarmiento<sup>1</sup>

<sup>1</sup>Atmospheric and Oceanic Sciences Program, Princeton University, Princeton, NJ, USA.

<sup>3</sup>Scripps Institution of Oceanography, University of California, San Diego, La Jolla, California, USA.

<sup>3</sup>Monterey Bay Aquarium Research Institute, Moss Landing, California, USA.

\*Corresponding author: F. Alexander Haumann (alexander.haumann@gmail.com)

### Key Points:

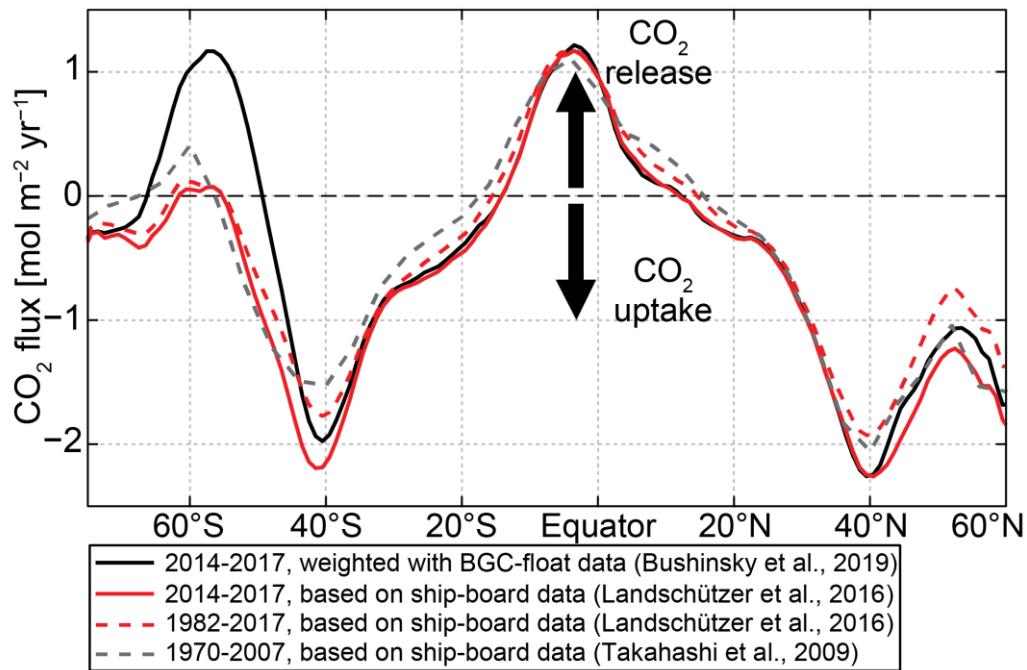
- Deep ocean CO<sub>2</sub> release arises from high potential CO<sub>2</sub> partial pressure in subsurface water between the Subantarctic Front and sea-ice edge
- Maximum subsurface potential CO<sub>2</sub> coincides with the outcrop of upwelling Indo-Pacific Deep Water, rich in remineralized organic carbon
- High alkalinity and low temperature prevent CO<sub>2</sub> release from high carbon-content deep water outcropping south of Indo-Pacific Deep Water

21 **Abstract**

22 The deep ocean naturally releases large amounts of old, pre-industrial carbon dioxide (CO<sub>2</sub>) to the  
23 atmosphere through upwelling in the Southern Ocean, closing the global ocean carbon cycle. This  
24 Southern Ocean CO<sub>2</sub> release is relevant to the global climate, because its changes could alter  
25 atmospheric CO<sub>2</sub> levels on long time scales and the present-day potential of the Southern Ocean  
26 to take up anthropogenic CO<sub>2</sub>. Here, based on observational data, we show that this CO<sub>2</sub> release  
27 arises from a zonal band of subsurface waters between the Subantarctic Front and wintertime sea-  
28 ice edge with a potential partial pressure of CO<sub>2</sub> exceeding current atmospheric CO<sub>2</sub> levels  
29 ( $\Delta\text{PCO}_2$ ) by 175  $\mu\text{atm}$ . This band of high  $\Delta\text{PCO}_2$  subsurface water coincides with the outcropping  
30 of the 27.8 kg m<sup>-3</sup> isoneutral density surface that marks the upwelling of Indo-Pacific Deep Water  
31 (IPDW). Vertically, the IPDW layer exhibits a distinct  $\Delta\text{PCO}_2$  maximum in the deep ocean, which  
32 is set by remineralization of organic carbon and originates from the northern Pacific and Indian  
33 Ocean basins. Below this IPDW layer, the carbon content increases downwards, whereas  $\Delta\text{PCO}_2$   
34 decreases. Most of this vertical  $\Delta\text{PCO}_2$  decline results from decreasing temperatures and increasing  
35 alkalinity due to an increased fraction of calcium carbonate dissolution. These two factors limit  
36 the CO<sub>2</sub> outgassing from the high-carbon content deep waters on more southerly surface outcrops.  
37 Our results imply that the response of Southern Ocean CO<sub>2</sub> fluxes to possible future changes in  
38 upwelling are sensitive to the subsurface carbon chemistry set by the vertical remineralization and  
39 dissolution profiles.

40 **1 Introduction**

41 Based on year-round biogeochemical measurements with profiling floats, recent work has  
 42 identified a larger than previously estimated release of carbon dioxide (CO<sub>2</sub>) from the Southern  
 43 Ocean to the atmosphere during austral winter (black line in Figure 1; Bushinsky et al., 2019; Gray  
 44 et al., 2018). While there has been a broad consensus that the region south of about 50°S releases  
 45 old, pre-industrial CO<sub>2</sub> to the atmosphere (Gruber et al., 2019; Mikaloff Fletcher et al., 2007;  
 46 Morrison et al., 2015; Wu et al., 2019), the magnitude and extent of this CO<sub>2</sub> release have been  
 47 substantially smaller in previous estimates, which were derived from ship-board measurements  
 48 (gray and red lines in Figure 1; Landschützer et al., 2016, 2020; Takahashi et al., 2009). These  
 49 smaller previous estimates largely arise from a lack of data during austral winter, when deep  
 50 mixing stirs waters with elevated partial pressure of CO<sub>2</sub> (*p*CO<sub>2</sub>) to the surface. In this study, we  
 51 analyze observations from ships and floats measured at depth that are not prone to large seasonal  
 52 variations in order to address the question if such a large outgassing from the Southern Ocean  
 53 during winter can be expected when deep waters are brought to the surface. We aim to further our  
 54 understanding of the underlying mechanisms of this deep ocean CO<sub>2</sub> release in the Southern Ocean  
 55 and to identify its sources.



56

57 **Figure 1.** Zonal and annual mean global ocean to atmosphere CO<sub>2</sub> flux (positive values denote  
 58 ocean CO<sub>2</sub> release to the atmosphere) from different data products for different time periods.

59 Black: Neural-network estimate, weighed with biogeochemical Argo float data (Bushinsky et al.,  
60 2019; Landschützer et al., 2019). Red: Neural-network estimate, based on ship-board observations  
61 from the SOCAT database (Landschützer et al., 2016, 2020). Gray: Climatology based on ship-  
62 board observations from the CDIAC database (Takahashi et al., 2009).

63 In the Southern Ocean (south of about 50°S), CO<sub>2</sub> is naturally released from the ocean to the  
64 atmosphere due to the upwelling of carbon-rich waters from the deep layers of the global ocean  
65 (Mikaloff Fletcher et al., 2007; Morrison et al., 2015; Takahashi et al., 2009; Wu et al., 2019).  
66 Globally, the Southern Ocean CO<sub>2</sub> release is balanced by CO<sub>2</sub> uptake in the subtropics and northern  
67 subpolar oceans (Figure 1; Gruber et al., 2009; Takahashi et al., 2002, 2009). This CO<sub>2</sub> uptake is  
68 driven in part by cooling of the surface water as it is being transported to higher latitudes, which  
69 increases its capacity to hold CO<sub>2</sub>, and in part by the sinking of biologically produced organic  
70 matter out of the surface layer (Gruber et al., 2009; Takahashi et al., 2002, 2009). The biologically  
71 produced organic carbon sinks through the thermocline and is being remineralized at depth, where  
72 it feeds the deep waters with inorganic carbon, which is then transported to the Southern Ocean  
73 (Sarmiento & Gruber, 2006). Therefore, the upwelling and CO<sub>2</sub> release in the Southern Ocean  
74 closes the global ocean carbon cycle.

75 The leakage of old, pre-industrial CO<sub>2</sub> from the deepest ocean layers is unique to the high-latitude  
76 Southern Ocean, because this is the only region where deep waters ascend to the surface along  
77 rising, steep isopycnals (Morrison et al., 2015; Speer et al., 2000; Talley, 2013; Toggweiler &  
78 Samuels, 1995). Deep waters exit the Indian, Pacific and Atlantic basins in both western and  
79 eastern boundary currents, and spiral southeastward and upward until reaching the base of the  
80 mixed layer in the southern Antarctic Circumpolar Current (ACC; Tamsitt et al., 2017, 2019). This  
81 upwelling process is thought to be the major return pathway for remineralized carbon from the  
82 ocean's interior to the surface (Kwon et al., 2009; Sarmiento et al., 1988; Skinner et al., 2010).  
83 Estimates of ocean transport show that a supply of dissolved inorganic carbon (DIC) to the  
84 Southern Ocean surface comes from a southward and upward flux of Circumpolar Deep Water  
85 (CDW; Iudicone et al., 2011; Wu et al., 2019). This southward transport consists of North Atlantic  
86 Deep Water (NADW), Lower Circumpolar Deep Water (LCDW) in the Indian and Pacific basins,  
87 and somewhat less dense Indo-Pacific Deep Water (IPDW) that all carry DIC from sinking and  
88 remineralization of biogenic carbon, and, in the case of NADW, DIC from air-sea gas exchange  
89 (Aldama-Campino et al., 2020; Broecker & Peng, 1992).

90 In this study, we seek to explain the characteristic meridional patterns of surface CO<sub>2</sub> fluxes in the  
91 Southern Ocean (Figure 1), to explain why CO<sub>2</sub> release peaks in a zonal band between 55°S and  
92 60°S, and to identify the pathway and sources of how the deep ocean loses carbon to the  
93 atmosphere. For this purpose, we assess factors that could affect the deep ocean's outgassing  
94 potential using subsurface DIC, alkalinity, and nutrient data from ship-based observations (Key et  
95 al., 2004, 2015; Lauvset et al., 2016; Olsen et al., 2016) and biogeochemical floats (Johnson et al.,  
96 2017). In order to relate these ocean observational data to the Southern Ocean surface CO<sub>2</sub> fluxes,  
97 in a first step, we here make use of the interior ocean potential  $p\text{CO}_2$  ( $\text{PCO}_2$ ; Broecker & Peng,  
98 1982; Skinner et al., 2010) excess above the approximate current (year 2015) global-mean  
99 atmospheric  $p\text{CO}_2$  ( $p\text{CO}_2^{\text{atm}} = 400 \mu\text{atm}$ ), i.e.  $\Delta\text{PCO}_2 = \text{PCO}_2 - p\text{CO}_2^{\text{atm}}$ . Thus, we calculate the  
100 seawater  $\text{PCO}_2$  as the  $p\text{CO}_2$  that a water parcel would attain if it were adiabatically brought to the  
101 surface (Broecker & Peng, 1982) using its DIC, alkalinity, potential temperature ( $\theta$ ) and sea-level  
102 pressure. The resulting  $\Delta\text{PCO}_2$  is then a more accurate measure of the capability of upwelling  
103 water to release CO<sub>2</sub> to the present-day atmosphere than DIC alone. In a second step, we analyze  
104 the drivers of the spatial patterns of  $\Delta\text{PCO}_2$  in the interior ocean by estimating the different  
105 contributions of the dissolution, solubility, gas exchange and biological carbon pump processes  
106 (Gruber & Sarmiento, 2002; Sarmiento & Gruber, 2006; Volk & Hoffert, 1985). In a third step,  
107 we decompose  $\Delta\text{PCO}_2$  vertical gradient into components associated with DIC, temperature, and  
108 alkalinity. Using this decomposition, we demonstrate the importance of considering the full  
109 vertical carbon chemistry structure, in particular alkalinity, when assessing the influence of the  
110 carbon-rich deep ocean on the surface Southern Ocean CO<sub>2</sub> fluxes.

## 111 **2 Methods**

### 112 **2.1 Potential $p\text{CO}_2$ and neutral density**

113 Potential  $p\text{CO}_2$  ( $\text{PCO}_2$ ) is defined as the  $p\text{CO}_2$  that a water parcel would attain if it was brought to  
114 the surface adiabatically (Broecker & Peng, 1982; Sarmiento & Gruber, 2006; Skinner et al.,  
115 2010), thus correcting for the pressure effects on temperature and partial pressure.  $\text{PCO}_2$  is  
116 computed following Williams et al. (2017) using CO2SYS (van Heuven et al., 2011) and by using  
117 dissociation constants of carbonate from Lueker et al. (2000), of sulfate from Dickson (1990), and  
118 of fluoride from Perez & Fraga (1987), and the boron to salinity ratio of Lee et al. (2010). Here,

119  $PCO_2$  is a function of alkalinity (Alk), DIC, potential temperature ( $\theta$ , referenced to 0 dbar),  
 120 practical salinity (S), the reference pressure ( $p^{ref} = 0$  dbar), silicate (Si), and phosphate ( $PO_4$ ). For  
 121 biogeochemical float data (section 3), we use nitrate ( $NO_3$ ) and convert it to  $PO_4$  and Si using  
 122 stoichiometric phosphate-to-nitrate and silicate-to-nitrate ratios of 1:16 and 2.5, respectively  
 123 (Anderson & Sarmiento, 1994). Note that we here use the deviation of the interior ocean  $PCO_2$   
 124 from the approximate current (year 2015) atmospheric  $pCO_2$  of  $400 \mu atm$  ( $\Delta PCO_2$ ) to illustrate the  
 125 present-day outgassing potential of an interior ocean water mass, which differs from past or future  
 126 atmospheric conditions.

127 We here evaluate the interior ocean  $\Delta PCO_2$  structure considering neutral density surfaces. For this  
 128 purpose, we have calculated the neutral density ( $\gamma^n$ ) for all data sets (section 3) based on Jackett &  
 129 McDougall (1997; version 3.05.12; 17<sup>th</sup> June, 2019; [http://www.teos-](http://www.teos-10.org/preteos10_software/neutral_density.html)  
 130 [10.org/preteos10\\_software/neutral\\_density.html](http://www.teos-10.org/preteos10_software/neutral_density.html)). Since in this code  $\gamma^n$  is not defined for  
 131 temperatures below  $-2.5$  °C, any possible temperature below this value is set to  $-2.5$  °C.

## 132 **2.2 Dilution and solubility**

133 In a first step, we estimate the effect of dilution of ocean tracers through freshwater fluxes on  $PCO_2$   
 134 ( $\Delta PCO_2^{dil}$ ) by evaluating the difference between  $PCO_2$  and  $sPCO_2$  derived from salinity  
 135 normalized (s) quantities:

$$136 \quad \Delta PCO_2^{dil} = PCO_2 - sPCO_2. \quad (1)$$

137 Here,  $sPCO_2$  is derived using  $sAlk$ ,  $sDIC$ ,  $sSi$ , and  $sPO_4$ , whereas salinity normalization of a given  
 138 variable X to a reference salinity ( $S^{ref} = 34.7$ ) is performed through (Broecker & Peng, 1992; Chen  
 139 & Millero, 1979)

$$140 \quad sX = \frac{X}{S} S^{ref}. \quad (2)$$

141 The only exception here is  $sDIC$ , which we obtain by first salinity normalizing its preindustrial  
 142 value and then adding the anthropogenic component (see section 3).

143 In a second step, we estimate the effect of solubility on the interior ocean  $PCO_2$  distribution  
 144 ( $\Delta PCO_2^{sol}$ ) through

$$145 \quad \Delta PCO_2^{sol} = sPCO_2 - PCO_2^{DIC,Alk}. \quad (3)$$

146 Here,  $\text{PCO}_2^{\text{DIC,Alk}}$  is the  $\text{PCO}_2$  arising from variations in  $\text{sDIC}$  and  $\text{sAlk}$  and it is computed as a  
 147 function of  $\text{sAlk}$ ,  $\text{sDIC}$ ,  $\theta^{\text{ref}}$  (2.5 °C),  $S^{\text{ref}}$  (34.7),  $p^{\text{ref}}$  (0 dbar),  $\text{sSi}$ , and  $\text{sPO}_4$ . Reference values  $\theta^{\text{ref}}$   
 148 and  $S^{\text{ref}}$  are arbitrary values that depend on the purpose of the analysis. The resulting  $\Delta\text{PCO}_2^{\text{sol}}$   
 149 provides a measure for the contribution of mostly temperature differences relative to the location  
 150 of the reference value. Since we are interested in the ocean interior structure of  $\text{PCO}_2$ , we chose  
 151 these reference values to reflect deep water properties. If e.g.  $\theta^{\text{ref}}$  was set to 20 °C, which is closer  
 152 to global surface water temperatures, the interior ocean  $\text{PCO}_2^{\text{DIC,Alk}}$  would become much larger  
 153 than the actual  $\text{PCO}_2$  and  $\Delta\text{PCO}_2^{\text{sol}}$  strongly negative everywhere.

### 154 **2.3 Biological pumps**

155 We further attribute the interior ocean  $\Delta\text{PCO}_2$  variations to the driving biological pump  
 156 components, i.e. the soft-tissue and carbonate pumps that are associated with the photosynthesis  
 157 and remineralization of organic matter as well as the precipitation and dissolution of calcium  
 158 carbonate ( $\text{CaCO}_3$ ), respectively. We make use of a concept that has been developed to separate  
 159 the interior ocean DIC variations into these contributions (Gruber & Sarmiento, 2002; Sarmiento  
 160 & Gruber, 2006; Volk & Hoffert, 1985) to estimate their effect on  $\Delta\text{PCO}_2$ . In order to achieve this  
 161 goal, we first separately estimate the  $\text{sDIC}$ ,  $\text{sAlk}$ ,  $\text{sPO}_4$  and  $\text{sSi}$  deviations from their global-mean  
 162 surface reference values, which are listed in Table 1, defined as  $\Delta X = \text{sX} - \text{sX}^{\text{ref}}$ , for any variable  
 163  $X$ . For  $\text{sDIC}^{\text{ref}}$ , we use the estimated pre-industrial surface mean value, since the effect of  
 164 anthropogenic carbon is estimated separately (sections 2.4 and 3). Since the surface ocean  $\text{sPO}_4$ ,  
 165 is most likely also affected by anthropogenic activity, we chose a  $\text{sPO}_4^{\text{ref}}$  that is lower than the  
 166 global mean surface value. We lower  $\text{sPO}_4^{\text{ref}}$  so that a small positive residual  $\Delta\text{PCO}_2$  residual in  
 167 the deep northern Pacific becomes zero. We expect this region to have a zero residual  $\Delta\text{PCO}_2$   
 168 because the effects of air-sea gas exchange, which are reflected by the residual (section 2.4), should  
 169 be negligible in the deep northern Pacific where waters have been isolated from the atmosphere for  
 170 thousands of years (Holzer et al., 2021). We note that  $\text{sPO}_4^{\text{ref}}$  value chosen here is also close to the  
 171 value used by Gruber & Sarmiento (2002).

172 **Table 1.** Reference values used in this study for the estimation of the drivers of interior ocean  
 173  $\text{PCO}_2$  variations, in part derived from gridded GLODAPv2 data (Lauvset et al., 2016).

| Variable         | Value  | Description        |
|------------------|--------|--------------------|
| $p^{\text{ref}}$ | 0 dbar | Reference pressure |

|                             |                              |  |
|-----------------------------|------------------------------|--|
| $S^{\text{ref}}$            | 34.7                         | Reference ocean salinity   |
| $\theta^{\text{ref}}$       | 2.5 °C                       | Reference ocean temperature  |
| $p\text{CO}_2^{\text{atm}}$ | 400 $\mu\text{atm}$          | Approximate atmospheric partial pressure of $\text{CO}_2$ in 2015              |
| $\text{PCO}_2^{\text{ref}}$ | 131 $\mu\text{atm}$          | Partial pressure of $\text{CO}_2$ using reference values of this table         |
| $s\text{Alk}^{\text{ref}}$  | 2298 $\mu\text{mol kg}^{-1}$ | Reference surface ocean alkalinity   |
| $s\text{PO}_4^{\text{ref}}$ | 0.1 $\mu\text{mol kg}^{-1}$  | Reference surface ocean phosphate concentration                                |
| $s\text{Si}^{\text{ref}}$   | 6.3 $\mu\text{mol kg}^{-1}$  | Reference surface ocean silicate concentration                                 |
| $s\text{DIC}^{\text{ref}}$  | 1967 $\mu\text{mol kg}^{-1}$ | Reference preindustrial surface ocean dissolved inorganic carbon concentration |

174 The contributions of the soft-tissue pump to the  $\Delta\text{DIC}$  and  $\Delta\text{Alk}$  are then estimated as

$$175 \quad \Delta\text{DIC}^{\text{soft}} = r_{\text{C:P}} \Delta\text{PO}_4, \quad (4)$$

176 and

$$177 \quad \Delta\text{Alk}^{\text{soft}} = -r_{\text{C:N}} \Delta\text{DIC}^{\text{soft}}, \quad (5)$$

178 respectively. Here,  $r_{\text{C:P}}$  and  $r_{\text{N:C}}$  are the carbon-to-phosphate and nitrate-to-carbon stoichiometric  
 179 ratios set to 117/1 and 16/117, respectively (Anderson & Sarmiento, 1994). The latter ratio is  
 180 applied because a molar increase in seawater nitrate due to e.g. the remineralization of organic  
 181 matter equals the molar decline in Alk (Sarmiento & Gruber, 2006).

182 Subsequently, the contributions of the carbonate pump to the  $\Delta\text{DIC}$  and  $\Delta\text{Alk}$  are estimated as

$$183 \quad \Delta\text{Alk}^{\text{carb}} = \Delta\text{Alk} - \Delta\text{Alk}^{\text{soft}}, \quad (6)$$

184 and

$$185 \quad \Delta\text{DIC}^{\text{carb}} = 0.5 \Delta\text{Alk}^{\text{carb}}, \quad (7)$$

186 respectively.

187 In contrast to DIC and Alk,  $\text{PCO}_2$  is not a conserved tracer but depends on current carbon chemistry  
 188 and solubility of the water. Therefore, separating  $\Delta\text{PCO}_2$  deviations into its components is not  
 189 straightforward. Nevertheless, we can quantify the range of values by calculating each  
 190 contribution, i.e.  $\Delta\text{PCO}_2^{\text{soft}}$  and  $\Delta\text{PCO}_2^{\text{carb}}$ , under four scenarios, during which we vary processes  
 191 that modify the  $\text{PCO}_2$  sensitivity to DIC and Alk, and using  $p^{\text{ref}}$ ,  $S^{\text{ref}}$ , and  $\theta^{\text{ref}}$ .

192 The first scenario for  $\Delta PCO_2^{soft}$  assumes that the soft-tissue pump is the only process influencing  
 193 DIC and Alk deviations from the reference values. As such,  $\Delta PCO_2^{soft}$  is calculated by using sDIC,  
 194 sAlk, sPO<sub>4</sub>, and sSi fields that are driven by the soft-tissue pump alone:

$$195 \quad \Delta PCO_2^{soft} = PCO_2(sDIC^{ref} + \Delta DIC^{soft}, sAlk^{ref} + \Delta Alk^{soft}, sPO_4, sSi) - PCO_2^{ref}. \quad (8)$$

196 where  $PCO_2^{ref}$  is the ocean  $PCO_2$  calculated using all reference values (Table 1). The second and  
 197 third scenarios assume that one of the two other processes influencing DIC and Alk, i.e. carbonate  
 198 pump and gas exchange (section 2.4), has occurred prior to the soft-tissue pump to determine the  
 199  $PCO_2$  sensitivity to DIC and Alk. Therefore, we quantify  $\Delta PCO_2^{soft}$  as the  $PCO_2$  difference between  
 200 when both the soft-tissue pump and carbonate pump are operating and that when only the carbonate  
 201 pump is active:

$$202 \quad \Delta PCO_2^{soft} = PCO_2(sDIC^{ref} + \Delta DIC^{carb} + \Delta DIC^{soft}, sAlk^{ref} + \Delta Alk^{carb} + \Delta Alk^{soft}, sPO_4, sSi) - PCO_2(sDIC^{ref} + \Delta DIC^{carb}, sAlk^{ref} + \Delta Alk^{carb}, sPO_4^{ref}, sSi^{ref}), \quad (9)$$

203 and as the  $PCO_2$  difference between when both the soft-tissue pump and gas exchange (including  
 204 the anthropogenic component) are operating and that when only gas exchange is active:

$$205 \quad \Delta PCO_2^{soft} = PCO_2(sDIC^{ref} + \Delta DIC^{gasex} + \Delta DIC^{cant} + \Delta DIC^{soft}, sAlk^{ref} + \Delta Alk^{soft}, sPO_4, sSi) - PCO_2(sDIC^{ref} + \Delta DIC^{gasex} + \Delta DIC^{cant}, sAlk^{ref}, sPO_4^{ref}, sSi^{ref}). \quad (10)$$

206 where  $\Delta DIC^{gasex}$  and  $\Delta DIC^{cant}$  are defined in sections 2.4 and 3, respectively. The last scenario is  
 207 that  $\Delta PCO_2^{soft}$  occurs after all the other processes to change the  $PCO_2$  sensitivity. Therefore, we  
 208 have

$$209 \quad \Delta PCO_2^{soft} = PCO_2(sDIC, sAlk, sPO_4, sSi) - PCO_2(sDIC - \Delta DIC^{soft}, sAlk - \Delta Alk^{soft}, sPO_4^{ref}, sSi^{ref}). \quad (11)$$

210 We then use the mean of the four scenarios (equations 8 to 11) as an estimate for the contribution  
 211 of the  $\Delta PCO_2^{soft}$  to the interior ocean  $\Delta PCO_2$  distribution.  $\Delta PCO_2^{carb}$  is estimated following the  
 212 same procedure.

## 213 **2.4 Air-sea gas exchange**

214 We proceed to estimate the effect of air-sea gas exchange on the interior ocean  $\Delta\text{PCO}_2$  distribution.  
 215 For this purpose, we separately consider the pre-industrial gas exchange ( $\Delta\text{DIC}^{\text{gasex}}$ ) and its  
 216 anthropogenic component, by using  $\Delta\text{DIC}^{\text{cant}}$  estimates (Lauvset et al., 2016; see section 3) and  
 217 calculating  $\Delta\text{DIC}^{\text{gasex}}$  as the residual of all other terms:

$$218 \quad \Delta\text{DIC}^{\text{gasex}} = s\text{DIC} - s\text{DIC}^{\text{ref}} - \Delta\text{DIC}^{\text{cant}} - \Delta\text{DIC}^{\text{soft}} - \Delta\text{DIC}^{\text{carb}}. \quad (12)$$

219 We then apply the same approach as outlined in equations 8 to 11, but replacing the soft-tissue  
 220 pump components with the respective gas exchange components, yielding estimates for  $\Delta\text{PCO}_2^{\text{gasex}}$   
 221 and  $\Delta\text{PCO}_2^{\text{cant}}$ .

## 222 **2.5 Impact of carbon chemistry and solubility on the vertical $\Delta\text{PCO}_2$ distribution**

223 To quantify how the water carbon chemistry and solubility effects drive the vertical  $\Delta\text{PCO}_2$   
 224 distribution, we separately estimate the departure of  $\Delta\text{PCO}_2$  due to deviations of DIC, Alk, and  $\theta$   
 225 and S, from the respective reference values (Table 1). The increasing DIC with depth is the primary  
 226 source of the elevated  $\Delta\text{PCO}_2$  in the deeper layers of the ocean, which is then modified by Alk,  $\theta$ ,  
 227 and S. Therefore, we first estimate  $\text{PCO}_2$  variations due to DIC alone ( $\Delta\text{PCO}_2^{\text{DIC}}$ ):

$$228 \quad \Delta\text{PCO}_2^{\text{DIC}} = \text{PCO}_2^{\text{DIC}} - \text{PCO}_2^{\text{ref}} = \text{PCO}_2(s\text{DIC}, s\text{Alk}^{\text{ref}}, \theta^{\text{ref}}, S^{\text{ref}}, s\text{PO}_4, s\text{Si}) - \text{PCO}_2^{\text{ref}}. \quad (13)$$

229 We then estimate the impact of Alk variations ( $\Delta\text{PCO}_2^{\text{Alk}}$ ) as

$$230 \quad \Delta\text{PCO}_2^{\text{Alk}} = \text{PCO}_2^{\text{DIC,Alk}} - \text{PCO}_2^{\text{DIC}} - \text{PCO}_2^{\text{ref}} \quad (14)$$

231 where,  $\text{PCO}_2^{\text{DIC,Alk}}$  is defined in section 2.2. Moreover, we define  $\Delta\text{PCO}_2^{\text{DIC,Alk}} = \text{PCO}_2^{\text{DIC,Alk}} -$   
 232  $p\text{CO}_2^{\text{atm}}$ .

## 233 **3 Data**

234 Our conclusions are drawn from ship-based measurements and measurements by profiling floats.  
 235 We use physical and biogeochemical data from the gridded Global Ocean Data Analysis Project  
 236 version 2 (GLODAPv2; Key et al., 2004, 2015; Lauvset et al., 2016; Olsen et al., 2016)  
 237 climatology, which are provided at a  $1^\circ$  by  $1^\circ$  spatial resolution. GLODAPv2 is based on shipboard  
 238 measurements from 724 hydrographic cruises from 1972 to 2013. Estimates of anthropogenic DIC

239 provided in the mapped GLODAPv2 data (Lauvset et al., 2016) were used to assess the  
240 anthropogenic contribution to DIC. The GLODAPv2 DIC and  $\Delta\text{DIC}^{\text{cant}}$  estimates are referenced  
241 to the year 2002. In addition, we use biogeochemical profiling float data from a broad region in  
242 the Southern Ocean (Johnson et al., 2021), which were deployed as part of the Southern Ocean  
243 Carbon and Climate Observations and Modeling (SOCCOM) project (Johnson et al., 2017). Here,  
244 we use a total of 8332 profiles from 174 floats with measurements of high-quality pH (Johnson et  
245 al., 2016; Williams et al., 2017),  $\text{NO}_3$ , and estimated Alk (Carter et al., 2018) to estimate  $\text{PCO}_2$ .

246 Surface  $\text{CO}_2$  flux data stems from two neural-network estimates; one is weighted towards  
247 biogeochemical Argo float data (Bushinsky et al., 2019; Landschützer et al., 2019) and one uses  
248 only shipboard observations from the SOCAT database (Landschützer et al., 2016, 2020). A third  
249 product is a climatology based on shipboard observations from the CDIAC database (Takahashi  
250 et al., 2009). Climatological frontal positions stem from Orsi et al. (1995) and the sea-ice edge  
251 position is the annual mean 1% sea-ice concentration from the merged product distributed through  
252 the Climate Data Record (1979 to 2018; Meier et al., 2017; Peng et al., 2013).

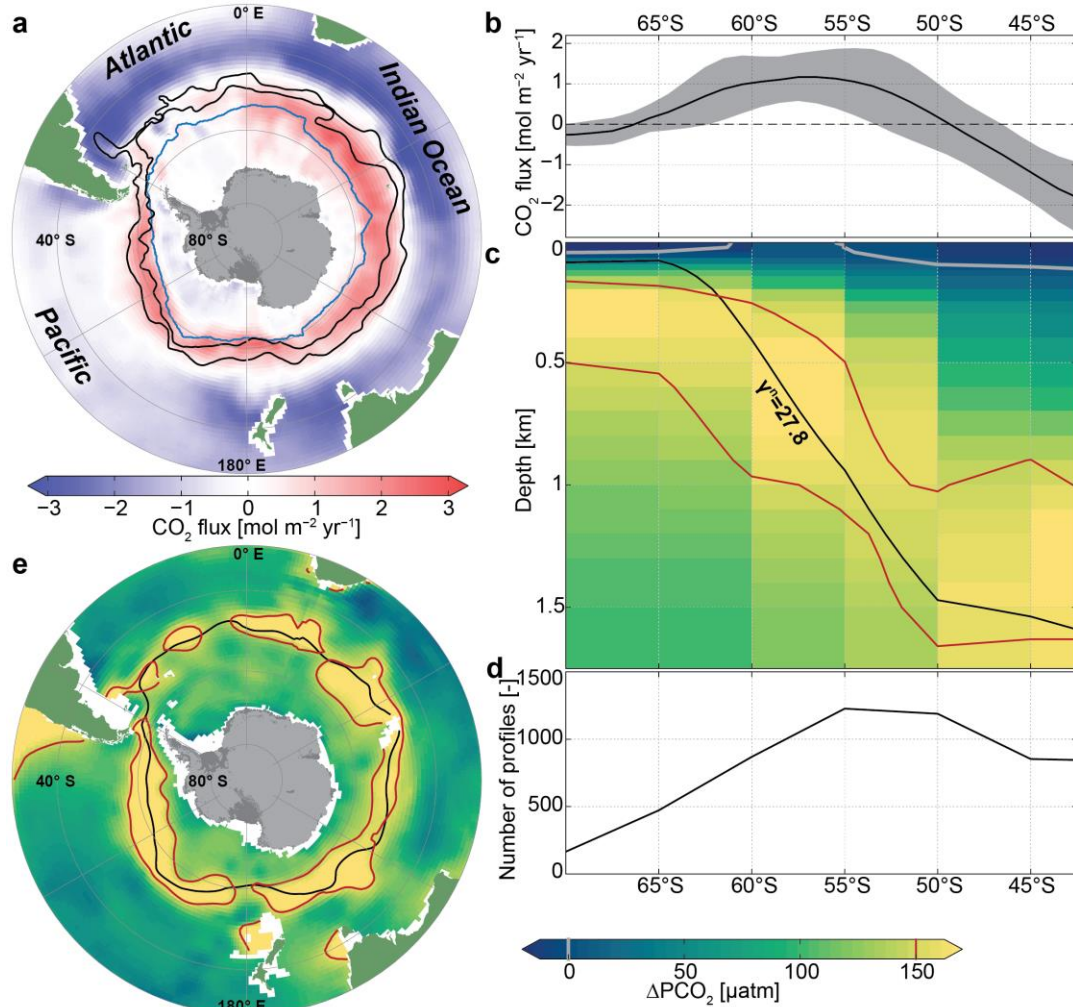
## 253 **4 Results**

### 254 **4.1 Spatial patterns of $\text{CO}_2$ release linked to subsurface $\Delta\text{PCO}_2$ maximum**

255 The float-weighted annual mean surface  $\text{CO}_2$  flux estimate (Bushinsky et al., 2019; Landschützer  
256 et al., 2019) reveals a distinct ring feature (Figure 2a,b), with strong  $\text{CO}_2$  release occurring within  
257 the ACC, roughly between the Subantarctic Front and the winter-time sea-ice edge. The highest  
258 outgassing occurs in the Pacific and Indian Ocean sectors, regionally exceeding  $3 \text{ mol m}^{-2} \text{ yr}^{-1}$   
259 (positive values are a  $\text{CO}_2$  flux from the ocean to the atmosphere; see also Prend et al., submitted).  
260 In these regions, intensive  $\text{CO}_2$  release is observed in the fall and winter, followed by weaker, yet  
261 non-negligible, outgassing fluxes in the remaining seasons (Bushinsky et al., 2019; Gray et al.,  
262 2018). North of the ACC,  $\text{CO}_2$  fluxes are characterized by a broad region of  $\text{CO}_2$  uptake. The  
263 highest annual uptake, below  $-3 \text{ mol m}^{-2} \text{ yr}^{-1}$ , is found in the Argentine Basin in the Atlantic,  
264 characterized by a strong uptake mostly occurring between spring to fall. In the seasonally ice-  
265 covered region, annual mean surface  $\text{CO}_2$  fluxes are generally small. In summary, the largest  $\text{CO}_2$   
266 release occurs roughly between the sea-ice edge and the Subantarctic Front during wintertime, a

267 region that is dominated by a wind-driven divergence at the surface and deep mixing in winter  
268 (Bushinsky et al., 2019; Gray et al., 2018; Prend et al., submitted).

269 The ring pattern of outgassing evident from the surface CO<sub>2</sub> fluxes aligns with the region of upward  
270 sloping isopycnal surfaces in the Southern Ocean subsurface between about 50°S and 65°S (Figure  
271 2c,d). In this region, the zonal mean ΔPCO<sub>2</sub> from the float profiles reveals a signature of high-  
272 ΔPCO<sub>2</sub> deep water that upwells along isopycnals. The vertical ΔPCO<sub>2</sub> maximum appears along the  
273 27.8 kg m<sup>-3</sup> neutral density surface, which shoals towards the south within the ACC; this is  
274 coincident with the core of the oxygen minimum layer that is characteristic of, and defines, IPDW  
275 (Talley, 2013; see also Figure 3g-i). The sign of the surface CO<sub>2</sub> fluxes (Figure 2b) closely tracks  
276 this the shoaling of the subsurface ΔPCO<sub>2</sub> maximum (Figure 2c), switching from CO<sub>2</sub> uptake north  
277 of 50°S to CO<sub>2</sub> outgassing between about 50°S and 65°S (Figure 2b). Maximum outgassing,  
278 between 55°S and 60°S, encompasses the latitude range of positive ΔPCO<sub>2</sub> at the surface (gray  
279 contour lines in Figure 2c). This picture of highest surface outgassing in the region where high-  
280 ΔPCO<sub>2</sub> waters upwell, as derived from the profiling floats, is corroborated by a ring pattern in the  
281 ΔPCO<sub>2</sub> constructed from gridded shipboard observations (section 3) at 800 m depth (Figure 2e). It  
282 reflects the high annual-mean surface CO<sub>2</sub> fluxes, with highest values occurring between the Polar  
283 and Subantarctic Front. The core of the subsurface high-ΔPCO<sub>2</sub> ring coincides with the  
284 outcropping of the 27.8 kg m<sup>-3</sup> neutral density surface (black in Figure 2c,e). Both the surface CO<sub>2</sub>  
285 fluxes and the subsurface ΔPCO<sub>2</sub> at 800 m decrease further south of the outcropping 27.8 kg m<sup>-3</sup>  
286 neutral density surface. Therefore, the reduced CO<sub>2</sub> outgassing south of its maximum is in part  
287 related to a decrease of the subsurface ΔPCO<sub>2</sub> south of 60°S. In addition, the inhibition of gas  
288 exchange by sea-ice cover, a potentially high biological carbon export efficiency (Arteaga et al.,  
289 2018), reduced mixing (Wilson et al., 2019), and cold surface temperatures could further limit the  
290 mixed-layer ΔPCO<sub>2</sub> and thereby surface CO<sub>2</sub> fluxes in this seasonally ice-covered region. In  
291 summary, the outcropping of the isopycnal surfaces in the Southern Ocean acts to project the  
292 vertical ΔPCO<sub>2</sub> structure with its maximum on the 27.8 kg m<sup>-3</sup> neutral density surface onto a  
293 horizontal plane, resulting in the meridional ΔPCO<sub>2</sub> maximum between the sea-ice edge and  
294 Subantarctic Front.



295

296 **Figure 2.** Southern Ocean CO<sub>2</sub> release and its subsurface source. **a**, Annual mean surface CO<sub>2</sub> flux  
 297 from a neural-network estimate that is weighted with biogeochemical Argo float data (Bushinsky  
 298 et al., 2019; Landschützer et al., 2019). Positive values (red) indicate CO<sub>2</sub> degassing from the  
 299 ocean to the atmosphere. Black contours denote the mean position of the Subantarctic and Polar  
 300 Fronts (Orsi et al., 1995). The light blue contour line represents the annual mean sea-ice edge (1%  
 301 mean sea-ice concentration). **b**, Zonally averaged annual mean surface CO<sub>2</sub> flux (as in panel a).  
 302 Gray shading denotes  $\pm 1$  standard deviation in the zonal direction. **c**, Zonally averaged annual-  
 303 mean potential  $p\text{CO}_2$  excess with respect to current atmospheric levels (400  $\mu\text{atm}$ ;  $\Delta\text{PCO}_2$ ) from  
 304 profiling floats (in 5° latitudinal bins). **d**, Number of float profiles per 5° latitudinal bins. **e**,  $\Delta\text{PCO}_2$   
 305 at 800 m from gridded GLODAPv2. In **c** and **e**, the 27.8 kg m<sup>-3</sup> isoneutral surface is shown in  
 306 black, and the 150  $\mu\text{atm}$  and 0  $\mu\text{atm}$   $\Delta\text{PCO}_2$  isolines in red and gray, respectively.

#### 307 4.2 Sources of the subsurface $\Delta\text{PCO}_2$ maximum

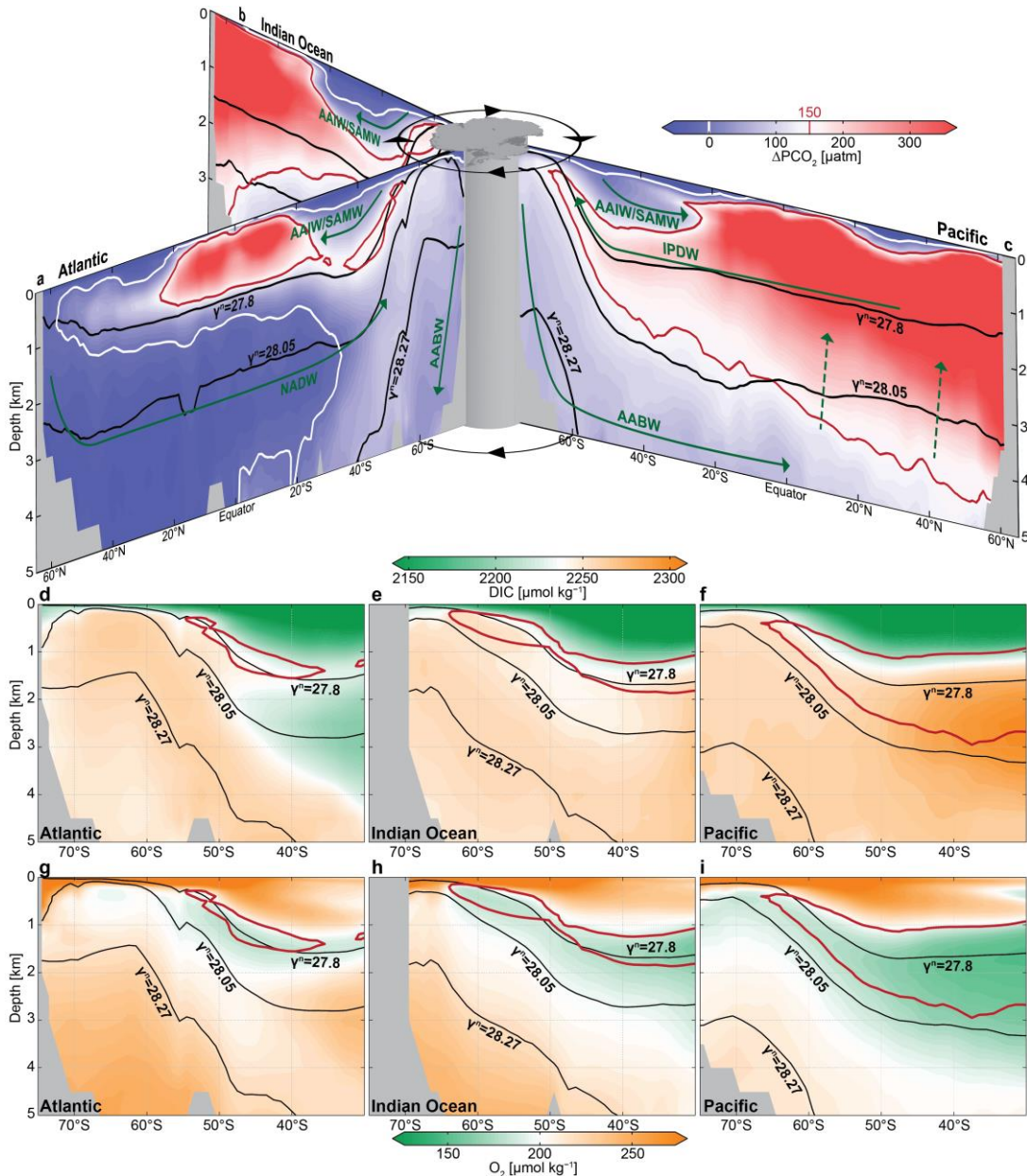
308 Where does the high subsurface  $\Delta\text{PCO}_2$  water in the Southern Ocean come from? In order to  
 309 address this question, in the following, we base our analysis  $\Delta\text{PCO}_2$  derived from a global data set

310 (GLODAPv2; Lauvset et al., 2016; see section 3) as displayed in Figure 3. Note that this data has  
311 several advantages, such as higher accuracy ship-board observations compared to the float data,  
312 actual alkalinity observations, and being a gridded product. However, major difference occur at  
313 the Southern Ocean surface. Here, the float data suggest an outcrop of the zero  $\Delta\text{PCO}_2$  contour  
314 (gray in Figure 2c), whereas the the zero  $\Delta\text{PCO}_2$  contour from ship-data (white in Figure 3a-c)  
315 does not outcrop. This difference most likely occurs from the lag of wintertime observations in  
316 GLODAPv2. In this study we are mostly interested in the subsurface  $\Delta\text{PCO}_2$ , where both data sets  
317 largely agree.

318 We now assume that, to a first order, water masses spread along isoneutral density surfaces  
319 (denoted as  $\gamma^N$ )—an assumption that has been widely used to identify the deep water circulation  
320 pathways (Jackett & McDougall, 1997). The  $\Delta\text{PCO}_2$  maximum follows the  $27.8 \text{ kg m}^{-3}$  isoneutral  
321 surface, which characterizes the IPDW core as identified by the vertical oxygen minimum (Talley,  
322 2013; Figure 3); hence the vertical oxygen and  $\Delta\text{PCO}_2$  extrema appear to have the same biological  
323 and physical forcing. The  $\Delta\text{PCO}_2$  maximum can be traced back from the Southern Ocean  
324 subsurface to its source region in the deep northern Indian and Pacific basins (Figure 3a-c). Here,  
325 the ocean is pervaded by  $\text{PCO}_2$ -rich waters, with  $\Delta\text{PCO}_2$  much larger than  $150 \mu\text{atm}$  extending  
326 from the thermocline to about 4 km depth (red contour line in Figure 3b,c).

327 The highest  $\Delta\text{PCO}_2$  waters, indicated by a  $\Delta\text{PCO}_2$  larger than  $800 \mu\text{atm}$ , are located in the North  
328 Pacific between  $50^\circ\text{N}$  and  $60^\circ\text{N}$  and between 500 m and 1500 m, where the oldest subsurface  
329 waters occur in the global ocean, supplied by slow vertical diffusion from below (dashed white  
330 lines in Figure 3c; Holzer et al., 2021; Talley, 2013). These waters with high  $\Delta\text{PCO}_2$  spread  
331 southward and outcrop at the sea surface in the Southern Ocean (Gent & McWilliams, 1990;  
332 Holzer et al., 2021; Talley, 2013). They enter the Southern Ocean as a layer of elevated  $\Delta\text{PCO}_2$   
333 that extends southward and upward across  $50^\circ\text{S}$ , where the zonal mean  $\text{PCO}_2$  exceeds atmospheric  
334 levels by about  $175 \mu\text{atm}$  (averaged between  $27.7 \text{ kg m}^{-3}$  and  $27.9 \text{ kg m}^{-3}$ ; Table 2). Both advective  
335 and diffusive eddy transport can play an important role in pulling these high  $\Delta\text{PCO}_2$  signals to the  
336 Southern Ocean subsurface (Dufour et al., 2015; Tamsitt et al., 2017), with the final step being  
337 entrainment into the surface mixed layer (Prend et al., submitted). This chimney of elevated  $\Delta\text{PCO}_2$   
338 is narrowly constrained along the IPDW core ( $27.8 \text{ kg m}^{-3}$  isoneutral surface; Figure 3c). As these  
339 waters reach the Southern Ocean, the  $\Delta\text{PCO}_2$  signal is strongly attenuated as a result of diapycnal

340 mixing with ambient low  $\Delta\text{PCO}_2$  waters, yet its magnitude is still strongly elevated and forms a  
 341 clear local vertical maximum. South of the Polar Front, where the  $27.8 \text{ kg m}^{-3}$  isoneutral surface  
 342 outcrops, the high  $\Delta\text{PCO}_2$  signals originated from the IPDW are circumpolarly distributed, again  
 343 mirroring the oxygen minimum layer (Figure 3g-i; Talley, 2013), and control the subsurface  
 344  $\Delta\text{PCO}_2$  around Antarctica.



345 **Figure 3.** Potential  $p\text{CO}_2$  excess above current atmospheric levels ( $400 \mu\text{atm}$ ;  $\Delta\text{PCO}_2$ ) and DIC in  
 346 the ocean interior from gridded GLODAPv2. Meridional sections of zonally averaged  $\Delta\text{PCO}_2$  in  
 347 the Atlantic (a), Indian Ocean (b), and Pacific (c), overlaid with a schematic representation of the  
 348 subsurface water pathways (white arrows) and the ACC (black arrows). Zonally averaged DIC in  
 349 the Atlantic (d), Indian (e), and Pacific (f) sectors of the Southern Ocean (south of  $30^\circ\text{S}$ ). Zonally  
 350

351 averaged dissolved oxygen ( $O_2$ ) in the Atlantic (**g**), Indian Ocean (**h**), and Pacific (**i**) sectors of the  
 352 Southern Ocean (south of  $30^\circ S$ ). Isonutral surfaces are shown in black ( $\gamma^N = 27.8$  and  $28.05$   $kg$   
 353  $m^{-3}$  characterizing IPDW and NADW, respectively), and the  $150$   $\mu atm$  and  $0$   $\mu atm$   $\Delta PCO_2$  isolines  
 354 in red and white, respectively.

355 In contrast to the maximum  $\Delta PCO_2$  found in IPDW, the lowest value of deep-ocean  $\Delta PCO_2$ , of  
 356 less than  $-50$   $\mu atm$ , is located in the northern Atlantic, where NADW is formed from surface  
 357 sources, and hence has higher oxygen and lower  $\Delta PCO_2$  than IPDW (Figure 3a,g). The NADW  
 358 core in the Southern Ocean has been identified by its salinity maximum, which roughly follows  
 359 the  $28.05$   $kg$   $m^{-3}$  isoneutral surface (Talley, 2013). While the  $\Delta PCO_2$  of NADW increases  
 360 continuously due to diapycnal mixing and biological processes as the NADW moves southward,  
 361 much less  $CO_2$  outgassing would be expected if NADW were the primary water mass being  
 362 ventilated in the Southern Ocean. In the Southern Ocean, NADW mixes with higher  $\Delta PCO_2$   
 363 LCDW from the Indo-Pacific (Figure 3c). Between  $45^\circ S$  and  $55^\circ S$ , the circumpolar average of  
 364 LCDW/NADW has a  $\Delta PCO_2$  that is about  $70$   $\mu atm$  lower than the  $\Delta PCO_2$  of IPDW (Table 2). This  
 365 LCDW/NADW mixture then upwells primarily in the region covered by the seasonal sea ice  
 366 (Talley, 2013), where the local environment further hinders the air-sea  $CO_2$  exchange. In  
 367 conclusion, our analysis shows that the characteristic pattern of a high  $\Delta PCO_2$  ring below the  
 368 mixed layer, which causes the Southern Ocean  $CO_2$  outgassing, is induced by the southward and  
 369 upward transport of IPDW through a narrow and relatively light isoneutral density band and cannot  
 370 be explained by the upwelling of LCDW, such as NADW.

### 371 **4.3 Drivers of high $\Delta PCO_2$ in Indo-Pacific Deep Water**

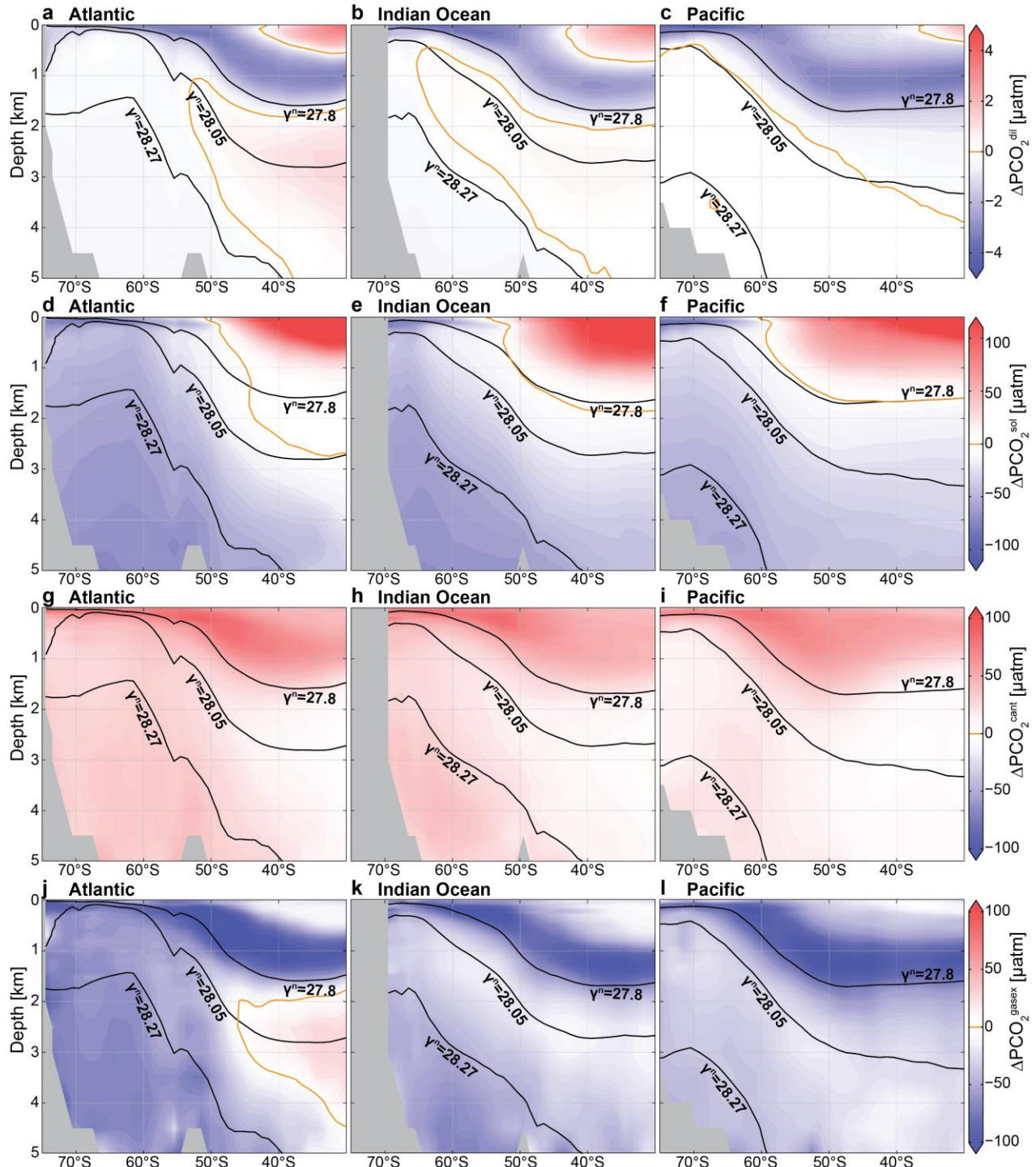
372 Why is  $\Delta PCO_2$  particularly elevated along the circulation pathway of IPDW? A larger  $CO_2$   
 373 outgassing potential in deep waters has generally been linked to a higher DIC content. However,  
 374 IPDW has no clear DIC maximum in the Southern Ocean (Figure 3d-f). Instead, vertically, the  
 375 DIC peaks are located at a much greater depth and higher density than those of  $\Delta PCO_2$ . For  
 376 example, DIC maxima in the Southern Ocean occur on isoneutral surfaces that are associated with  
 377 the Antarctic Bottom Water (AABW;  $\gamma^N \sim 28.27$   $kg$   $m^{-3}$ ; Orsi et al., 1999) in the Atlantic and  
 378 Indian Ocean (Figure 3d,e), and on isoneutral density surfaces of about  $28.0$   $kg$   $m^{-3}$  in the Pacific  
 379 north of  $50^\circ S$  (Figure 3f). Since the IPDW  $\Delta PCO_2$  maximum cannot simply be explained by its  
 380 carbon content (DIC), we here consider the different physical (dilution, solubility, air-sea gas

381 exchange; section 4.3.1) and biological processes (soft tissue and carbonate pumps; section 4.3.2),  
 382 as well as the carbonate chemistry (DIC, Alk; section 4.3.3) that determine the interior Southern  
 383 Ocean  $\text{PCO}_2$  structure (see section 2 for methods). For this purpose, we evaluate these  
 384 contributions on depth levels (Figures 4, 5, and 6a,b) and on neutral density surfaces that represent  
 385 the corresponding water masses (Figure 6c,d and Table 2). We vertically separate the subsurface  
 386 ocean into three neutral density layers: IPDW ( $27.7 \text{ kg m}^{-3} - 27.9 \text{ kg m}^{-3}$ ), LCDW/NADW ( $27.9$   
 387  $\text{kg m}^{-3} - 28.2 \text{ kg m}^{-3}$ ), AABW ( $> 28.2 \text{ kg m}^{-3}$ ; Figure 6 and Table 2).

#### 388 *4.3.1 Physical drivers of interior ocean $\Delta\text{PCO}_2$ structure*

389 Physical effects on  $\Delta\text{PCO}_2$  include the dilution of ocean tracers by surface freshwater fluxes,  
 390 changes in  $\text{CO}_2$  solubility due to variations in the interior ocean temperature and salinity structure,  
 391 and air-sea gas exchange (section 2.2). Dilution effects ( $\Delta\text{PCO}_2^{\text{dil}}$ ; Figure 4a-c, Table 2) are  
 392 generally small ( $< 5 \mu\text{atm}$ ). Compared to our chosen reference salinity of 34.7, the LCDW/NADW  
 393 layer ( $\gamma^N \sim 28.05 \text{ kg m}^{-3}$ ) and the subtropical surface waters have an elevated  $\Delta\text{PCO}_2^{\text{dil}}$  due to  
 394 evaporation effects on those waters. Antarctic surface waters, Antarctic Intermediate Water  
 395 (AAIW), and Subantarctic Mode Water (SAMW) experience a reduced  $\Delta\text{PCO}_2^{\text{dil}}$  due to a net  
 396 freshwater input at the Southern Ocean surface. However, this pattern cannot explain the overall  
 397 interior ocean  $\Delta\text{PCO}_2$  structure and its magnitude is negligible.

398 Solubility effects ( $\Delta\text{PCO}_2^{\text{sol}}$ ; Figure 4d-f), which are mostly associated with the interior Southern  
 399 Ocean temperature distribution and to a lesser degree with the salinity distribution, are on the order  
 400 of about 20 to 100  $\mu\text{atm}$ . They become very large in the much warmer subtropical thermocline  
 401 waters. Overall, the colder temperatures in the deepest layers, in particular AABW, as well as the  
 402 high-latitude Antarctic surface waters, reduce  $\Delta\text{PCO}_2$  and enhance the ability of these waters to  
 403 hold  $\text{CO}_2$  or reduce their outgassing potential. Thus, solubility effects have a substantial influence  
 404 on the interior Southern Ocean  $\Delta\text{PCO}_2$  structure and act to contribute to the observed vertical  
 405  $\Delta\text{PCO}_2$  decline, especially in the deepest layers (Figure 6a,b; Table 2). However, vertical  $\Delta\text{PCO}_2^{\text{sol}}$   
 406 gradients around the  $\Delta\text{PCO}_2$  maximum ( $27.8 \text{ kg m}^{-3}$ ) are weaker than in the abyssal ocean,  
 407 suggesting that other processes control the  $\Delta\text{PCO}_2$  decrease with depth, especially between the  
 408 IPDW and LCDW/NADW layers.



409  
 410 **Figure 4.** Physical drivers of the subsurface  $\Delta\text{PCO}_2$  structure. **a–c**, Dilution effects ( $\Delta\text{PCO}_2^{\text{dil}}$ )  
 411 relative to a salinity of 34.7. **d–f**, Solubility effects ( $\Delta\text{PCO}_2^{\text{sol}}$ ) with respect to a reference  
 412 temperature and salinity of 2.5 °C and 34.7, respectively. **g–i**, Influence of anthropogenic carbon  
 413 uptake ( $\Delta\text{PCO}_2^{\text{cant}}$ ). **j–l**, Influence of air-sea gas exchange ( $\Delta\text{PCO}_2^{\text{gasex}}$ ). Panels show the Atlantic

414 (left), Indian (middle), and Pacific (right) sectors of the Southern Ocean. Isoneutral surfaces are  
 415 shown in black, and the 0  $\mu\text{atm}$   $\Delta\text{PCO}_2$  isoline in orange.

416 For the effect of  $\text{CO}_2$  air-sea gas exchange on  $\Delta\text{PCO}_2$ , we split it into its anthropogenic ( $\Delta\text{PCO}_2^{\text{cant}}$ ;  
 417 Figure 4g-i) and natural ( $\Delta\text{PCO}_2^{\text{gasex}}$ ; Figure 4j-l) components, where  $\Delta\text{PCO}_2^{\text{cant}}$  is based on the  
 418 estimate of the anthropogenic carbon content as provided by GLODAPv2 (section 2.4).  $\Delta\text{PCO}_2^{\text{cant}}$   
 419 is elevated in the AAIW, SAMW, and subtropical surface waters and also has some smaller  
 420 positive values in the AABW (Gruber et al., 2019). However, a substantial amount of  $\Delta\text{PCO}_2^{\text{cant}}$   
 421 is also found in IPDW, and the decline of  $\Delta\text{PCO}_2^{\text{cant}}$  with depth contributes to the overall vertical  
 422  $\Delta\text{PCO}_2$  decline below IPDW (Table 2). Such an invasion of  $\Delta\text{PCO}_2^{\text{cant}}$  to the IPDW layer could  
 423 arise from along-isopycnal stirring by mesoscale eddies, connecting the surface outcrop of the  
 424 isopycnal with the older, upwelling deep waters (Abernathey & Ferreira, 2015).  $\Delta\text{PCO}_2^{\text{gasex}}$  is  
 425 largely negative, except in the NADW core (Figure 4j-l). These negative values reflect  $\text{CO}_2$   
 426 outgassing when waters are at the surface (Gruber et al., 2009). The most negative values of  
 427  $\Delta\text{PCO}_2^{\text{gasex}}$  are associated with AAIW. This water was formed by transforming the upwelling  
 428 IPDW into lighter waters at the Southern Ocean surface, mostly through freshening by sea ice and  
 429 precipitation (Haumann et al., 2016). While it was at the surface it has experienced a substantial  
 430 loss of  $\text{CO}_2$  to the atmosphere (Figure 2a) before the water was subducted as AAIW. Similarly to  
 431 its anthropogenic component, natural gas exchange effects also reach into the IPDW layer ( $\gamma^{\text{N}} \sim$   
 432  $27.8 \text{ kg m}^{-3}$ ). The negative peak of  $\Delta\text{PCO}_2^{\text{gasex}}$  just above the  $27.8 \text{ kg m}^{-3}$  isoneutral surface  
 433 contributes to the sharp decline of  $\Delta\text{PCO}_2$  just above the IPDW layer, but counteracts the decline  
 434 below this layer (Figure 6, Table 2). In summary, solubility effects and anthropogenic carbon  
 435 enforce, and gas-exchange counteracts the IPDW  $\Delta\text{PCO}_2$  maximum (Table 2).

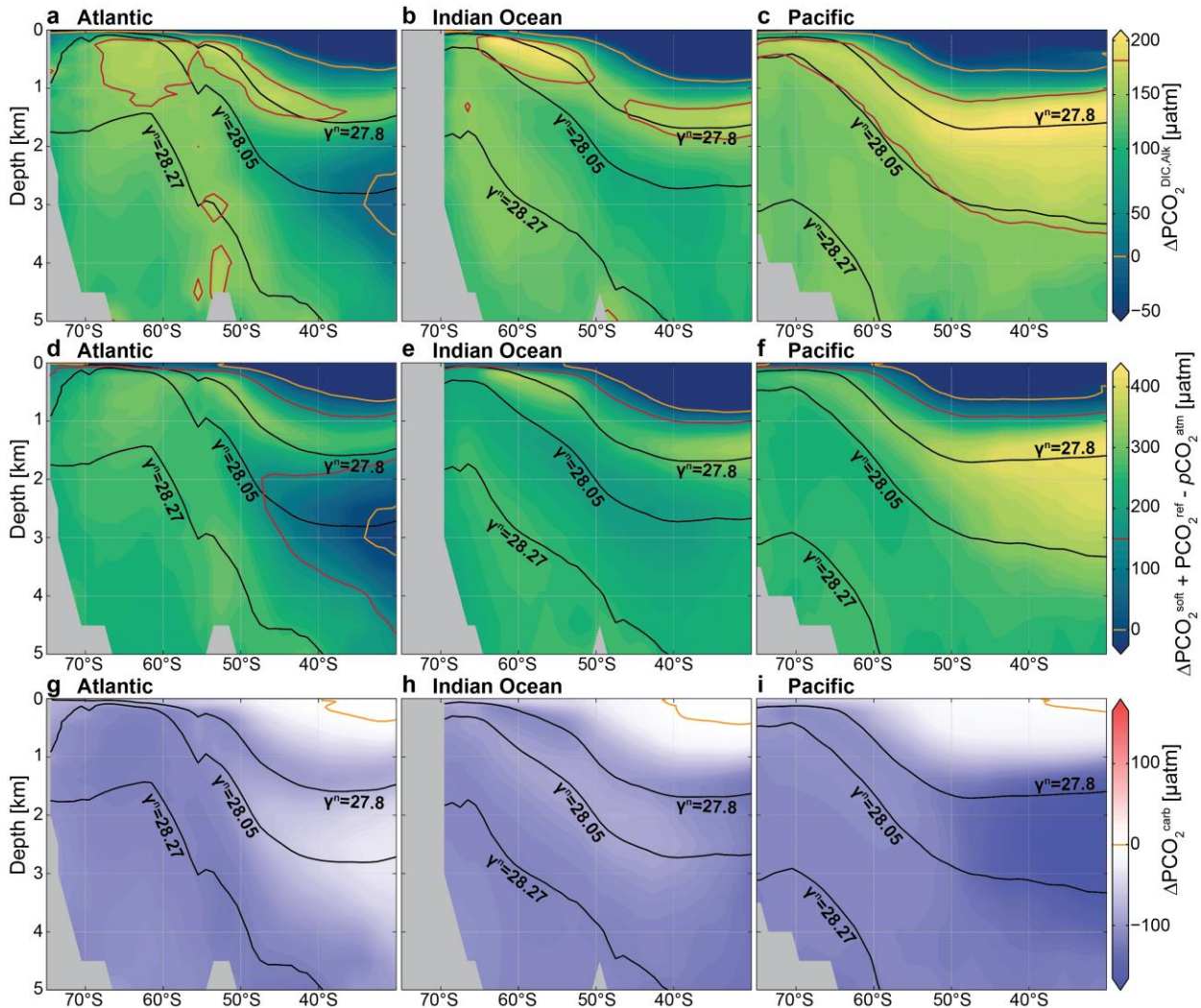
#### 436 *4.3.2 Biological drivers of interior ocean $\Delta\text{PCO}_2$ structure*

437 In order to better understand the biological contribution to the subsurface  $\Delta\text{PCO}_2$  structure in the  
 438 Southern Ocean, we compare the soft-tissue ( $\Delta\text{PCO}_2^{\text{soft}}$ ) and carbonate ( $\Delta\text{PCO}_2^{\text{carb}}$ ) pump  
 439 contributions to  $\Delta\text{PCO}_2$  variations arising from variations in sDIC and sAlk alone ( $\Delta\text{PCO}_2^{\text{DIC,Alk}}$ ;  
 440 Figure 5a-c), i.e. for fixed reference values of temperature, salinity, and pressure (section 2). Note  
 441 that  $\Delta\text{PCO}_2^{\text{DIC,Alk}}$  equals the sum of  $\text{PCO}_2^{\text{ref}}$ ,  $\Delta\text{PCO}_2^{\text{soft}}$ ,  $\Delta\text{PCO}_2^{\text{carb}}$ ,  $\Delta\text{PCO}_2^{\text{gasex}}$ , and  $\Delta\text{PCO}_2^{\text{cant}}$   
 442 minus  $p\text{CO}_2^{\text{atm}}$  (section 2). The soft-tissue pump ( $\Delta\text{PCO}_2^{\text{soft}}$ ) is the most efficient mechanism to  
 443 increase the deep ocean's  $\Delta\text{PCO}_2$  through the accumulation of remineralized carbon (DIC; Figure

444 6 and Table 2). The contribution of this mechanism to  $\Delta\text{PCO}_2$  explains most of the interior ocean  
 445 structure of  $\Delta\text{PCO}_2^{\text{DIC,Alk}}$  (Figure 5a-f), as well as the occurrence of very high  $\Delta\text{PCO}_2^{\text{DIC,Alk}}$  in  
 446 IPDW. High values of  $\Delta\text{PCO}_2^{\text{soft}}$  in the rather shallow IPDW (595  $\mu\text{atm}$ ; Table 2), as compared to  
 447 the deeper LCDW/NADW (506  $\mu\text{atm}$ ; Table 2), partially occur because IPDW accumulates  
 448 respired carbon over much longer timescales than the relatively younger NADW (DeVries &  
 449 Primeau, 2011), which is related to the long route that newly-ventilated AABW takes through the  
 450 Indian and Pacific, upwelling diffusively to produce IPDW, which then returns to the Southern  
 451 Ocean surface (Holzer et al., 2021; Talley, 2013). In addition to the difference in accumulation  
 452 time, IPDW receives more organic carbon from remineralization as a result of its rather shallow  
 453 depth in the water column (shallower than 1500 m) compared to LCDW/NADW and AABW  
 454 (Kwon et al., 2009; Martin et al., 1987). The organic matter received by IPDW could be about  
 455 twice as large as in the layers below when using a vertical organic carbon remineralization curve  
 456 that follows a classic power-law relationship (Martin et al., 1987) and ignoring possible spatial  
 457 differences in the production of organic matter at the surface. A secondary peak in both  
 458  $\Delta\text{PCO}_2^{\text{DIC,Alk}}$  and  $\Delta\text{PCO}_2^{\text{soft}}$  occurs around the 28.27  $\text{kg m}^{-3}$  isoneutral surface, which marks the  
 459 upper bound of AABW (Orsi et al., 1999), in particular in the Weddell Sea (Atlantic south of 50°S;  
 460 Figure 5a,d). This secondary  $\Delta\text{PCO}_2^{\text{DIC,Alk}}$  peak arises from local production and remineralization  
 461 within the Weddell Gyre (MacGilchrist et al., 2019). In conclusion,  $\Delta\text{PCO}_2^{\text{soft}}$  dominates the  
 462 vertical  $\Delta\text{PCO}_2$  decline below IPDW, which also explains the collocation between the vertical  
 463  $\Delta\text{PCO}_2$  maximum and the dissolved oxygen minimum in the deep ocean (section 4.2), because  
 464 also both quantities are dominated by the soft-tissue pump.

465 The magnitude of  $\Delta\text{PCO}_2^{\text{soft}}$  (Figure 5d-f) is substantially larger than  $\Delta\text{PCO}_2^{\text{DIC,Alk}}$  (Figure 5a-c),  
 466 because the carbonate pump ( $\Delta\text{PCO}_2^{\text{carb}}$ ; Figure 5g-i) counters the soft-tissue pump effect on  
 467  $\Delta\text{PCO}_2^{\text{DIC,Alk}}$ . This negative  $\Delta\text{PCO}_2^{\text{carb}}$  in the deep ocean arises from the dissolution of mineral  
 468 carbonates, which increases alkalinity twice as much as it increases DIC. The most negative values  
 469 of  $\Delta\text{PCO}_2^{\text{carb}}$  are located in the deep Pacific (Figure 5i), where dissolution of mineral carbonate is  
 470 enhanced by the metabolic  $\text{CO}_2$  release that drives the deep water to be undersaturated with respect  
 471 to calcite (Broecker & Peng, 1987; Jiang et al., 2015; Kwon et al., 2011; Sarmiento et al., 1988).  
 472 As the dissolution process strongly depends on pressure and preferentially happens at greater depth  
 473 compared to organic matter remineralization (Broecker & Peng, 1987; Kwon et al., 2011;

474 Sarmiento et al., 1988), the  $\Delta\text{PCO}_2^{\text{carb}}$  deficit appears to peak at greater depth than the  $\Delta\text{PCO}_2^{\text{soft}}$   
 475 maximum in the Pacific (Figure 5i). However, due to compensatory effects between the Atlantic  
 476 and the Pacific basins (Figure 5g,i), the  $\Delta\text{PCO}_2^{\text{carb}}$  contribution to the overall zonal mean vertical  
 477  $\Delta\text{PCO}_2$  decline with depth is small (Figure 6a; between 45°S and 55°S) and even of opposite sign  
 478 when averaged over neutral density layers (Table 2). Therefore, the overall effects of  $\Delta\text{PCO}_2^{\text{carb}}$  in  
 479 setting the vertical  $\Delta\text{PCO}_2$  maximum in IPDW are small, but are critical to understand the  
 480 differences between the vertical  $\Delta\text{PCO}_2$  and DIC profiles, as we show in the following section.

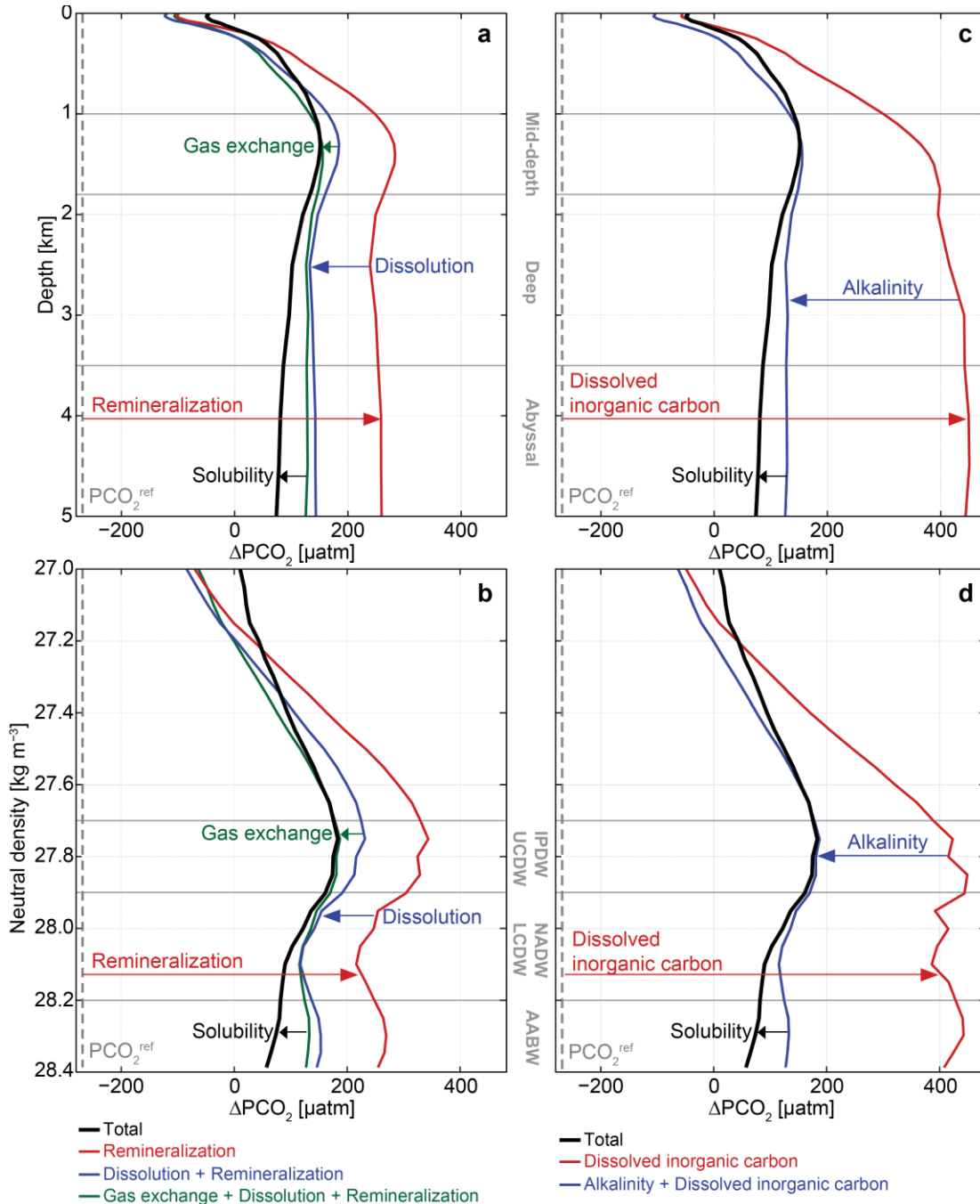


481  
 482 **Figure 5.** Biological drivers of the subsurface  $\Delta\text{PCO}_2$  structure. **a–c**,  $\Delta\text{PCO}_2$  structure due to  
 483 interior ocean DIC and Alk variations alone ( $\Delta\text{PCO}_2^{\text{DIC,Alk}}$ ), after removing dilution and solubility  
 484 effects. **d–f**, Expected  $\Delta\text{PCO}_2$  driven by the soft-tissue pump ( $\Delta\text{PCO}_2^{\text{soft}}$ ) due to photosynthesis  
 485 and remineralization of organic matter plus  $\text{PCO}_2^{\text{ref}}$  (131.5  $\mu\text{atm}$ ) minus  $p\text{CO}_2^{\text{atm}}$  (400  $\mu\text{atm}$ ). **g–i**,  
 486 Carbonate pump ( $\Delta\text{PCO}_2^{\text{carb}}$ ) due to precipitation and dissolution of calcium carbonate. Panels  
 487 show the Atlantic (left), Indian (middle), and Pacific (right) sectors of the Southern Ocean.

488 Isoneutral surfaces are shown in black, and the 150  $\mu\text{atm}$  and 0  $\mu\text{atm}$   $\Delta\text{PCO}_2$  isolines in red and  
489 orange, respectively.

#### 490 *4.3.3 Vertical difference between DIC and $\Delta\text{PCO}_2$ maxima between 45°S and 55°S*

491 We now separately consider the effects of DIC and alkalinity on the vertical  $\Delta\text{PCO}_2$  structure  
492 (Figure 6c,d) to better understand why  $\Delta\text{PCO}_2$  decreases below the 27.8  $\text{kg m}^{-3}$  isoneutral surface  
493 despite an equally high or higher carbon content (DIC) below this layer in the Southern Ocean  
494 (Figure 3). While the soft-tissue and carbonate pumps both act to enhance the DIC storage in the  
495 interior ocean, the carbonate pump adds DIC to a greater depth than the soft-tissue pump (Broecker  
496 & Peng, 1987; Kwon et al., 2011; Sarmiento et al., 1988). The difference between the vertical  
497  $\Delta\text{PCO}_2$  and DIC structure then largely results from the vertical alkalinity structure, since the soft-  
498 tissue pump decreases the deep ocean alkalinity (increasing  $\Delta\text{PCO}_2$ ) and the carbonate pump  
499 increases it (decreasing  $\Delta\text{PCO}_2$ ). This impact of alkalinity on the zonal mean vertical  $\Delta\text{PCO}_2$   
500 structure between 45°S and 55°S is shown in Figure 6c,d (see section 2.5). Compared to the  $\Delta\text{PCO}_2$   
501 maximum of 175  $\mu\text{atm}$  in IPDW,  $\Delta\text{PCO}_2$  in LCDW/NADW waters is 70  $\mu\text{atm}$  lower (Table 2).  
502 The largest contributor to this reduction, i.e. 30  $\mu\text{atm}$ , is alkalinity, while the remainder is  
503 explained by a colder temperature and lower DIC (Table 2; Figure 6d). The DIC contribution arises  
504 from low-DIC NADW, which vanishes in depth coordinates, where Alk and temperature effects  
505 are the sole drivers of the vertical  $\Delta\text{PCO}_2$  decline with depth (Figure 6c). These roles of alkalinity  
506 and temperature in driving a vertical  $\Delta\text{PCO}_2$  decline become even larger when comparing the  
507 IPDW layer to AABW. Thus, the vertical DIC gradient cannot explain the lower  $\Delta\text{PCO}_2$  in deeper  
508 and heavier waters, except for the NADW core ( $\gamma^N \sim 28.05 \text{ kg m}^{-3}$ ), where it contributes. In  
509 conclusion, the separation between the deeper DIC and shallower  $\Delta\text{PCO}_2$  maxima is caused by the  
510 shallower depth of remineralization of organic carbon compared to the depth of dissolution of  
511 calcium carbonate that sets the relative contributions of DIC and Alk in driving  $\Delta\text{PCO}_2$ ,  
512 corroborated by a decreasing temperature with depth.



513  
514  
515  
516  
517  
518

**Figure 6.** Drivers of the vertical  $\Delta\text{PCO}_2$  profile between 45°S and 55°S. Decomposition of  $\Delta\text{PCO}_2$  profiles into biological and physical processes in (a) depth and (b) neutral density coordinates. Decomposition of  $\Delta\text{PCO}_2$  profiles into chemical (DIC, Alk) and physical components in (c) depth and (d) neutral density coordinates. Note that in this figure, for simplicity, gas exchange is the combination of anthropogenic and natural components and dilution effects are neglected.

519 **Table 2.** Deep ocean  $\Delta\text{PCO}_2$  (in  $\mu\text{atm}$ ) and its estimated sources averaged for different water  
 520 masses (columns 2, 3, 4) and differences between water masses and IPDW (columns 5, 6).

| Layer            | IPDW   | LCDW/NADW  | AABW                         | LCDW/NADW<br>–<br>IPDW | AABW<br>–<br>IPDW |
|------------------|--|--|------------------------------|------------------------|-------------------|
| Range            | 27.7 kg m <sup>-3</sup> –<br>27.9 kg m <sup>-3</sup> | 27.9 kg m <sup>-3</sup> –<br>28.2 kg m <sup>-3</sup> | > 28.2 kg<br>m <sup>-3</sup> |                        |                   |
| Total            | 175  | 104  | 77                           | -70                    | -97               |
| Dilution         | -1   | 0  | 0                            | 2                      | 1                 |
| Solubility       | -4   | -23  | -53                          | -19                    | -48               |
| Remineralization | 595  | 506  | 530                          | -89                    | -65               |
| Dissolution      | -112   | -104   | -114                         | 8                      | -2                |
| Anthropogenic    | 39   | 18   | 25                           | -21                    | -13               |
| Gas exchange     | -78  | -25  | -46                          | 53                     | 33                |
| DIC              | 657  | 634  | 665                          | -23                    | 8                 |
| Alkalinity       | -249   | -279   | -307                         | -30                    | -58               |

## 521 5 Conclusions and discussion

522 We here show that the upwelling of high- $\Delta\text{PCO}_2$  IPDW occurs along the 27.8 kg m<sup>-3</sup> isoneutral  
 523 surface in the Southern Ocean, which we identify as the major global pathway for old, pre-  
 524 industrial carbon to return to the surface and as the key source of Southern Ocean outgassing. The  
 525 importance of this isopycnal and pathway for supply of old, nutrient-rich IPDW to the surface of  
 526 the Southern Ocean was previously identified through the location of the IPDW oxygen minimum  
 527 (Talley, 2013). Here we highlight its relevance of being the major return pathway of CO<sub>2</sub> from the  
 528 deep ocean to the atmosphere. This pathway draws from a high- $\Delta\text{PCO}_2$  pool in the mid-depth  
 529 northern Indo-Pacific basins, which exceeds current atmospheric CO<sub>2</sub> levels (400  $\mu\text{atm}$ ) by more  
 530 than 800  $\mu\text{atm}$  and is the result of a slow accumulation of carbon due to the remineralization of  
 531 organic matter. The resulting high-PCO<sub>2</sub> IPDW propagates southward, where it subsequently  
 532 upwells in the high-latitude Southern Ocean, retaining a high- $\Delta\text{PCO}_2$  signal that exceeds current  
 533 atmospheric levels by 175  $\mu\text{atm}$ . Our findings thus provide observational evidence that there is a  
 534 substantial transport of old, pre-industrial CO<sub>2</sub> from the deep ocean to the atmosphere through the  
 535 Southern Ocean surface under present-day conditions. Therefore, interior ocean measurements  
 536 support the recent argument for a large natural CO<sub>2</sub> release at the surface in the open waters around  
 537 Antarctica (Bushinsky et al., 2019; Gray et al., 2018), sourced from relatively high PCO<sub>2</sub> water  
 538 that has upwelled to just beneath the mixed layer; this outgassing signal is best observed in winter  
 539 when deep mixing entrains the high- $\Delta\text{PCO}_2$  IPDW to the surface (Prend et al., submitted).

540 We find that the vertical subsurface  $\Delta\text{PCO}_2$  gradient, and in particular the isopycnal that best  
541 characterizes its subsurface maximum, directly controls the meridional pattern of the Southern  
542 Ocean surface  $\text{CO}_2$  fluxes. The maximum outgassing between the Subantarctic Front and the  
543 winter-time sea-ice edge is caused by a circumpolar band of high- $\Delta\text{PCO}_2$  IPDW just beneath the  
544 surface mixed layers. This characteristic ring pattern of Southern Ocean outgassing and high  
545 subsurface  $\Delta\text{PCO}_2$  is due to the southward-rising isopycnal surfaces that project the vertical  
546  $\Delta\text{PCO}_2$  maximum in IPDW onto the horizontal plane. The ring is circumpolar because the deep  
547 waters spiral southeastward with the ACC while they are rising, and are thus found all around  
548 Antarctica even though the original sources are localized boundary outflows from the Indian and  
549 Pacific basins (Tamsitt et al., 2017). Denser waters, such as NADW, reach the surface south of the  
550 maximum outgassing region in the ACC, and do not considerably contribute to the outgassing due  
551 to their lower  $\Delta\text{PCO}_2$ . Thus, the vertical  $\Delta\text{PCO}_2$  distribution at mid-latitudes directly explains the  
552 characteristic ring structure of Southern Ocean  $\text{CO}_2$  release (Figure 2a,e).

553 Deep ocean carbon content (DIC) is often used as a measure for Southern Ocean  $\text{CO}_2$  release.  
554 However, we here have shown that only considering upwelling DIC can lead to misinterpretations,  
555 since the subsurface DIC structure critically differs from the subsurface  $\Delta\text{PCO}_2$  structure that  
556 controls the surface  $\text{CO}_2$  fluxes. The DIC maximum occurs much deeper in the water column and  
557 remains high all the way to the bottom of the ocean, whereas  $\Delta\text{PCO}_2$  peaks shallower and declines  
558 with depth. In our analysis, we show that the vertical distribution of  $\Delta\text{PCO}_2$  and dissolved oxygen  
559 in the deep ocean are controlled primarily by the soft-tissue pump, whereas the vertical distribution  
560 of DIC is influenced by both the soft-tissue and the carbonate pumps, offsetting its maximum to  
561 deeper layers. This elevated carbon content (DIC) in the denser and deeper water masses, such as  
562 LCDW and AABW, is buffered by their carbon chemistry (high alkalinity) and colder  
563 temperatures, which prevents  $\text{CO}_2$  outgassing from these waters. This reduced outgassing potential  
564 from higher alkalinity in the deeper waters is the result of a deeper depth of calcium carbonate  
565 dissolution compared to organic matter remineralization in the global ocean, which has been  
566 identified as a key mechanism for actively retaining carbon at depth over long time scales  
567 (Broecker & Peng, 1987; Hain et al., 2010; Krumhardt et al., 2020; Kwon et al., 2011; Toggweiler,  
568 1999). Consequently, next to an adequate ocean circulation, a realistic representation of the vertical  
569 remineralization and dissolution profiles in the global ocean is an important pre-requisite for Earth

570 System Models to accurately simulate Southern Ocean CO<sub>2</sub> fluxes and the global ocean carbon  
571 cycle, as well as their response to climatic changes.

572 Model simulations project an enhanced future upwelling of deep waters in the Southern Ocean  
573 (Downes & Hogg, 2013) due to a poleward intensification of westerly winds (Bracegirdle et al.,  
574 2020) and changes in the surface buoyancy forcing (Bishop et al., 2016; Downes et al., 2018).  
575 Such an increased upwelling could substantially amplify the leakage of pre-industrial CO<sub>2</sub> from  
576 the deep ocean (Lovenduski et al., 2007; Toggweiler & Russell, 2008) and lead to a “saturation”  
577 of the anthropogenic CO<sub>2</sub> uptake by the ocean (Lovenduski et al., 2007; Le Quéré et al., 2007).  
578 However, there is still limited confidence in future projections of upwelling in the Southern Ocean  
579 (Meredith et al., 2019) since these models do not resolve mesoscale eddies (Bishop et al., 2016;  
580 Meredith et al., 2012; Morrison & Hogg, 2013) that are important for the ocean’s carbon transport  
581 (Abernathey & Ferreira, 2015; Dufour et al., 2015) and suffer from large biases in their water mass  
582 structure (Beadling et al., 2020; Downes et al., 2018). In addition, global climate models struggle  
583 to produce the correct patterns and magnitudes (Lenton et al., 2013; Mongwe et al., 2018) and  
584 temporal variability (Gruber et al., 2019) of surface CO<sub>2</sub> fluxes in the Southern Ocean.  
585 Observational evidence derived from chlorofluorocarbon measurements points towards an  
586 increased upwelling since the early 1990s (Ting & Holzer, 2017; Waugh et al., 2013). However,  
587 recent findings also show that the relation between upwelling deep waters and changes in the  
588 surface CO<sub>2</sub> fluxes is much more complex and exhibits strong fluctuations on decadal time scales  
589 (DeVries et al., 2019; Landschützer et al., 2015). Our results imply that not only the strength of  
590 circulation changes in the Southern Ocean plays an important role in altering the release of CO<sub>2</sub>  
591 from the deep ocean to the atmosphere, but also the depth level from which waters are upwelled.  
592 Moreover, they also imply that changes in subsurface carbon chemistry could impact the deep  
593 ocean CO<sub>2</sub> release. These implications of our results highlight the importance of improving the  
594 subsurface carbon chemistry, water-mass structure, and circulation in global climate models in  
595 order to better assess future changes in atmospheric CO<sub>2</sub> in response to ocean circulation changes.

## 596 **Acknowledgments**

597 All data and tools underlying this analysis are openly available: Mapped GLODAP version 2  
598 (<https://www.glodap.info/index.php/mapped-data-product>; [https://doi.org/10.5194/essd-8-325-](https://doi.org/10.5194/essd-8-325-2016)  
599 [2016](https://doi.org/10.5194/essd-8-325-2016)); SOCCOM float data (Snapshot 2021-05-05; <https://doi.org/10.6075/J0T43SZG>); globally

600 mapped CO<sub>2</sub> flux estimate based on the Surface Ocean CO<sub>2</sub> Atlas Database (SOCAT) and  
 601 Southern Ocean Carbon and Climate Observations and Modeling (SOCCOM) biogeochemistry  
 602 floats (1982 to 2017, NCEI Accession 0191304, Version 2.2; <https://doi.org/10.25921/9hsn-xq82>);  
 603 Global monthly gridded sea surface pCO<sub>2</sub> product from 1982 onward and its monthly climatology  
 604 (NCEI Accession 0160558, Version 5.5; <https://doi.org/10.7289/V5Z899N6>); CDIAC CO<sub>2</sub>  
 605 flux estimated from air-sea difference in CO<sub>2</sub> partial pressure (revised October 2009;  
 606 [https://www.ldeo.columbia.edu/res/pi/CO2/carbondioxide/pages/air\\_sea\\_flux\\_2010.html](https://www.ldeo.columbia.edu/res/pi/CO2/carbondioxide/pages/air_sea_flux_2010.html));  
 607 MATLAB Program Developed for CO<sub>2</sub> System Calculations  
 608 ([https://doi.org/10.3334/CDIAC/otg.CO2SYS\\_MATLAB\\_v1.1](https://doi.org/10.3334/CDIAC/otg.CO2SYS_MATLAB_v1.1)); NOAA/NSIDC Climate Data  
 609 Record of Passive Microwave Sea Ice Concentration (Version 3, 1979-2018;  
 610 <https://doi.org/10.7265/N59P2ZTG>).

611 This work was sponsored by NSF's Southern Ocean Carbon and Climate Observations and  
 612 Modeling (SOCCOM, PLR-1425989) Project under the NSF Award PLR-1425989, supplemented  
 613 by NASA (NNX14AP49G), and by the International Argo Program and the NOAA programs that  
 614 contribute to it. H.C. was supported by SOCCOM. F.A.H. was supported by the SNSF grant  
 615 numbers P2EZP2\_175162 and P400P2\_186681. K.S.J. thanks support from the David and Lucile  
 616 Packard Foundation through the Monterey Bay Aquarium Research Institute. We are deeply  
 617 thankful to Robert Key, Siv Lauvset, Are Olsen, and the large number of scientists, technicians,  
 618 and funding agencies responsible for the collection and quality control of the high-quality ship-  
 619 based data in GLODAPv2 (<https://www.glodap.info/index.php/group>) and for providing a gridded  
 620 data product that underpins much of this work. We thank Joan Llort, Daniel Sigman, and Robert  
 621 Toggweiler for comments and discussion on an earlier version of this paper.

622 **Author contributions:** H.C., F.A.H., and J.L.S. designed the study. H. C. and F.A.H conducted  
 623 the analysis. F.A.H. and H.C. wrote the paper supported by J.L.S.. All authors discussed the results  
 624 and contributed ideas.

## 625 References

- 626 Abernathey, R., & Ferreira, D. (2015). Southern Ocean isopycnal mixing and ventilation changes  
 627 driven by winds. *Geophysical Research Letters*, 42(23), 10357–10365.  
 628 <https://doi.org/10.1002/2015GL066238>
- 629 Aldama-Campino, A., Fransner, F., Ödalen, M., Groeskamp, S., Yool, A., Döös, K., & Nycander,  
 630 J. (2020). Meridional Ocean Carbon Transport. *Global Biogeochemical Cycles*, 34(9),

- 631 e2019GB006336. <https://doi.org/10.1029/2019GB006336>
- 632 Anderson, L. A., & Sarmiento, J. L. (1994). Redfield ratios of remineralization determined by  
633 nutrient data analysis. *Global Biogeochemical Cycles*, 8(1), 65–80.  
634 <https://doi.org/10.1029/93GB03318>
- 635 Arteaga, L., Haëntjens, N., Boss, E., Johnson, K. S., & Sarmiento, J. L. (2018). Assessment of  
636 Export Efficiency Equations in the Southern Ocean Applied to Satellite-Based Net Primary  
637 Production. *Journal of Geophysical Research: Oceans*, 123(4), 2945–2964.  
638 <https://doi.org/10.1002/2018JC013787>
- 639 Beadling, R. L., Russell, J. L., Stouffer, R. J., Mazloff, M., Talley, L. D., Goodman, P. J., et al.  
640 (2020). Representation of Southern Ocean properties across Coupled Model Intercomparison  
641 Project generations: CMIP3 to CMIP6. *Journal of Climate*, 33(15), 6555–6581.  
642 <https://doi.org/10.1175/jcli-d-19-0970.1>
- 643 Bishop, S. P., Gent, P. R., Bryan, F. O., Thompson, A. F., Long, M. C., Abernathey, R., et al.  
644 (2016). Southern Ocean Overturning Compensation in an Eddy-Resolving Climate  
645 Simulation. *Journal of Physical Oceanography*, 46(5), 1575–1592.  
646 <https://doi.org/10.1175/JPO-D-15-0177.1>
- 647 Bracegirdle, T. J., Krinner, G., Tonelli, M., Haumann, F. A., Naughten, K. A., Rackow, T., et al.  
648 (2020). Twenty first century changes in Antarctic and Southern Ocean surface climate in  
649 CMIP6. *Atmospheric Science Letters*. <https://doi.org/10.1002/asl.984>
- 650 Broecker, W. S., & Peng, T.-H. (1987). The Role of CaCO<sub>3</sub> Compensation in the Glacial to  
651 Interglacial Atmospheric CO<sub>2</sub> Change. *Global Biogeochemical Cycles*, 1(1), 15–29.  
652 Retrieved from <http://dx.doi.org/10.1029/GB001i001p00015>
- 653 Broecker, W. S., & Peng, T. H. (1982). *Tracers in the sea*. Eldigio Press.  
654 [https://doi.org/10.1016/0016-7037\(83\)90075-3](https://doi.org/10.1016/0016-7037(83)90075-3)
- 655 Broecker, W. S., & Peng, T. H. (1992). Interhemispheric transport of carbon dioxide by ocean  
656 circulation. *Nature*, 356(6370), 587–589. <https://doi.org/10.1038/356587a0>
- 657 Bushinsky, S. M., Landschützer, P., Rödenbeck, C., Gray, A. R., Baker, D., Mazloff, M. R., et al.  
658 (2019). Reassessing Southern Ocean Air-Sea CO<sub>2</sub> Flux Estimates With the Addition of  
659 Biogeochemical Float Observations. *Global Biogeochemical Cycles*, 33(11), 1370–1388.  
660 <https://doi.org/10.1029/2019GB006176>
- 661 Carter, B. R., Feely, R. A., Williams, N. L., Dickson, A. G., Fong, M. B., & Takeshita, Y. (2018).  
662 Updated methods for global locally interpolated estimation of alkalinity, pH, and nitrate.  
663 *Limnology and Oceanography: Methods*, 16(2), 119–131.  
664 <https://doi.org/10.1002/lom3.10232>
- 665 Chen, G. T., & Millero, F. J. (1979). Gradual increase of oceanic CO<sub>2</sub>. *Nature*, 277(5693), 205–  
666 206. <https://doi.org/10.1038/277205a0>
- 667 DeVries, T., & Primeau, F. (2011). Dynamically and Observationally Constrained Estimates of  
668 Water-Mass Distributions and Ages in the Global Ocean. *Journal of Physical Oceanography*,  
669 41(12), 2381–2401. <https://doi.org/10.1175/JPO-D-10-05011.1>
- 670 DeVries, T., Le Quéré, C., Andrews, O., Berthet, S., Hauck, J., Ilyina, T., et al. (2019). Decadal

- 671 trends in the ocean carbon sink. *Proceedings of the National Academy of Sciences*, 116(24),  
672 201900371. <https://doi.org/10.1073/pnas.1900371116>
- 673 Dickson, A. G. (1990). Standard potential of the reaction :  $\text{AgCl} (s) + 1/2\text{H}_2(g) = \text{Ag} (s) + \text{HCl}$   
674  $(aq)$ , and the standard acidity constant of the ion  $\text{HSO}_4^-$  in synthetic sea water from 273 .  
675 15 to 318 . 15 K. *The Journal of Chemical Thermodynamics*, 22(3), 113–127.
- 676 Downes, S. M., & Hogg, A. M. (2013). Southern Ocean Circulation and Eddy Compensation in  
677 CMIP5 Models. *Journal of Climate*, 26(18), 7198–7220. <https://doi.org/10.1175/JCLI-D-12-00504.1>
- 678
- 679 Downes, S. M., Spence, P., & Hogg, A. M. (2018). Understanding variability of the Southern  
680 Ocean overturning circulation in CORE-II models. *Ocean Modelling*, 123, 98–109.  
681 <https://doi.org/10.1016/j.ocemod.2018.01.005>
- 682 Dufour, C. O., Griffies, S. M., de Souza, G. F., Frenger, I., Morrison, A. K., Palter, J. B., et al.  
683 (2015). Role of Mesoscale Eddies in Cross-Frontal Transport of Heat and Biogeochemical  
684 Tracers in the Southern Ocean. *Journal of Physical Oceanography*, 45(12), 3057–3081.  
685 <https://doi.org/10.1175/JPO-D-14-0240.1>
- 686 Gent, P. R., & McWilliams, J. C. (1990). Isopycnal Mixing in Ocean Circulation Models. *Journal*  
687 *of Physical Oceanography*, 20(1), 150–155. [https://doi.org/10.1175/1520-0485\(1990\)020<0150:IMIOCM>2.0.CO;2](https://doi.org/10.1175/1520-0485(1990)020<0150:IMIOCM>2.0.CO;2)
- 688
- 689 Gray, A. R., Johnson, K. S., Bushinsky, S. M., Riser, S. C., Russell, J. L., Talley, L. D., et al.  
690 (2018). Autonomous Biogeochemical Floats Detect Significant Carbon Dioxide Outgassing  
691 in the High-Latitude Southern Ocean. *Geophysical Research Letters*, 45(17), 9049–9057.  
692 <https://doi.org/10.1029/2018GL078013>
- 693 Gruber, N., & Sarmiento, J. L. (2002). *Large scale biochemical/physical interactions in elemental*  
694 *cycles. The Sea: biological-physical interactions in the oceans* (Vol. 12).
- 695 Gruber, N., Gloor, M., Mikaloff Fletcher, S. E., Doney, S. C., Dutkiewicz, S., Follows, M. J., et  
696 al. (2009). Oceanic sources, sinks, and transport of atmospheric CO<sub>2</sub>. *Global Biogeochemical*  
697 *Cycles*, 23(1), GB1005. <https://doi.org/10.1029/2008GB003349>
- 698 Gruber, N., Landschützer, P., & Lovenduski, N. S. (2019). The Variable Southern Ocean Carbon  
699 Sink. *Annual Review of Marine Science*, 11(1), 159–186. <https://doi.org/10.1146/annurev-marine-121916-063407>
- 700
- 701 Hain, M. P., Sigman, D. M., & Haug, G. H. (2010). Carbon dioxide effects of Antarctic  
702 stratification, North Atlantic Intermediate Water formation, and subantarctic nutrient  
703 drawdown during the last ice age: Diagnosis and synthesis in a geochemical box model.  
704 *Global Biogeochemical Cycles*, 24(4), GB4023---. <https://doi.org/10.1029/2010GB003790>
- 705 Haumann, F. A., Gruber, N., Münnich, M., Frenger, I., & Kern, S. (2016). Sea-ice transport driving  
706 Southern Ocean salinity and its recent trends. *Nature*, 537(7618), 89–92.  
707 <https://doi.org/10.1038/nature19101>
- 708 van Heuven, S., Pierrot, D., Rae, J. W. B., Lewis, E., & Wallace, D. W. R. (2011). MATLAB  
709 Program Developed for CO<sub>2</sub> System Calculations. *ORNL/CDIAC-105b. Carbon Dioxide*  
710 *Information Analysis Center, Oak Ridge National Laboratory, U.S. Department of Energy,*  
711 *Oak Ridge, Tennessee.* [https://doi.org/10.3334/CDIAC/otg.CO2SYS\\_MATLAB\\_v1.1](https://doi.org/10.3334/CDIAC/otg.CO2SYS_MATLAB_v1.1)

- 712 Holzer, M., DeVries, T., & Lavergne, C. de. (2021). Diffusion controls the ventilation of a Pacific  
 713 Shadow Zone above abyssal overturning. *Nature Communications*, 12(1), 1–13.  
 714 <https://doi.org/10.1038/s41467-021-24648-x>
- 715 Iudicone, D., Rodgers, K. B., Stendardo, I., Aumont, O., Madec, G., Bopp, L., et al. (2011). Water  
 716 masses as a unifying framework for understanding the Southern Ocean Carbon Cycle.  
 717 *Biogeosciences*, 8(5), 1031–1052. <https://doi.org/10.5194/bg-8-1031-2011>
- 718 Jackett, D. R., & McDougall, T. J. (1997). A Neutral Density Variable for the World’s Oceans.  
 719 *Journal of Physical Oceanography*, 27(2), 237–263. [https://doi.org/10.1175/1520-0485\(1997\)027<0237:ANDVFT>2.0.CO;2](https://doi.org/10.1175/1520-0485(1997)027<0237:ANDVFT>2.0.CO;2)
- 721 Jiang, L., Feely, R. A., Carter, B. R., Greeley, D. J., Gledhill, D. K., & Arzayus, K. M. (2015).  
 722 Global Biogeochemical Cycles saturation state in the global oceans. *Global Biogeochemical*  
 723 *Cycles*, 29(10), 1656–1673. <https://doi.org/10.1002/2015GB005198>.Received
- 724 Johnson, K. S., Jannasch, H. W., Coletti, L. J., Elrod, V. A., Martz, T. R., Takeshita, Y., et al.  
 725 (2016). Deep-Sea DuraFET: A Pressure Tolerant pH Sensor Designed for Global Sensor  
 726 Networks. *Analytical Chemistry*, 88(6), 3249–3256.  
 727 <https://doi.org/10.1021/acs.analchem.5b04653>
- 728 Johnson, K. S., Plant, J. N., Coletti, L. J., Jannasch, H. W., Sakamoto, C. M., Riser, S. C., et al.  
 729 (2017). Biogeochemical sensor performance in the SOCCOM profiling float array. *Journal*  
 730 *of Geophysical Research: Oceans*. <https://doi.org/10.1002/2017JC012838>
- 731 Johnson, K. S., Riser, S. C., Boss, E. S., Talley, L. D., Sarmiento, J. L., Swift, D. D., et al. (2021).  
 732 SOCCOM float data - Snapshot 2021-05-05. In *Southern Ocean Carbon and Climate*  
 733 *Observations and Modeling (SOCCOM) Float Data Archive*. UC San Diego Library Digital  
 734 Collections. <https://doi.org/10.6075/J0T43SZG>
- 735 Key, R. M., Kozyr, A., Sabine, C. L., Lee, K., Wanninkhof, R., Bullister, J. L., et al. (2004). A  
 736 global ocean carbon climatology: Results from Global Data Analysis Project (GLODAP).  
 737 *Global Biogeochemical Cycles*, 18(4), GB4031. <https://doi.org/10.1029/2004GB002247>
- 738 Key, R. M., Olsen, A., Heuven, S. van, Lauvset, S. K., Velo, A., Lin, X., et al. (2015). Global  
 739 Ocean Data Analysis Project, Version 2 (GLODAPv2), ORNL/CDIAC-162, ND-P093. Oak  
 740 Ridge, Tennessee: Carbon Dioxide Information Analysis Center, Oak Ridge National  
 741 Laboratory, US Department of Energy.  
 742 [https://doi.org/10.3334/CDIAC/OTG.NDP093\\_GLODAPv2](https://doi.org/10.3334/CDIAC/OTG.NDP093_GLODAPv2)
- 743 Krumhardt, K. M., Long, M. C., Lindsay, K., & Levy, M. N. (2020). Southern Ocean Calcification  
 744 Controls the Global Distribution of Alkalinity. *Global Biogeochemical Cycles*, 34(12),  
 745 e2020GB006727. <https://doi.org/10.1029/2020GB006727>
- 746 Kwon, E. Y., Primeau, F., & Sarmiento, J. L. (2009). The impact of remineralization depth on the  
 747 air-sea carbon balance. *Nature Geoscience*, 2(9), 630–635. <https://doi.org/10.1038/ngeo612>
- 748 Kwon, E. Y., Sarmiento, J. L., Toggweiler, J. R., & DeVries, T. (2011). The control of atmospheric  
 749 pCO<sub>2</sub> by ocean ventilation change: The effect of the oceanic storage of biogenic carbon.  
 750 *Global Biogeochemical Cycles*, 25(3), GB3026. <https://doi.org/10.1029/2011GB004059>
- 751 Landschützer, P., Gruber, N., Haumann, F. A., Rödenbeck, C., Bakker, D. C. E., Heuven, S. Van,  
 752 et al. (2015). The reinvigoration of the Southern Ocean carbon sink. *Science*, 349, 1221–1224.

- 753 <https://doi.org/10.1126/science.aab2620>
- 754 Landschützer, P., Gruber, N., & Bakker, D. C. E. (2016). Decadal variations and trends of the  
755 global ocean carbon sink. *Global Biogeochemical Cycles*, 30(10), 1396–1417.  
756 <https://doi.org/10.1002/2015GB005359>
- 757 Landschützer, P., Bushinsky, S., & Gray, A. R. (2019). A combined globally mapped CO<sub>2</sub> flux  
758 estimate based on the Surface Ocean CO<sub>2</sub> Atlas Database (SOCAT) and Southern Ocean  
759 Carbon and Climate Observations and Modeling (SOCCOM) biogeochemistry floats from  
760 1982 to 2017 (NCEI Accession 0191304). Version 2.2. NOAA National Centers for  
761 Environmental Information. <https://doi.org/10.25921/9hsn-xq82>
- 762 Landschützer, P., Gruber, N., & Bakker, D. C. E. (2020). An observation-based global monthly  
763 gridded sea surface pCO<sub>2</sub> product from 1982 onward and its monthly climatology (NCEI  
764 Accession 0160558). Version 5.5. NOAA National Centers for Environmental Information.  
765 <https://doi.org/10.7289/V5Z899N6>
- 766 Lauvset, S. K., Key, R. M., Olsen, A., Van Heuven, S., Velo, A., Lin, X., et al. (2016). A new  
767 global interior ocean mapped climatology: The 1° × 1° GLODAP version 2. *Earth System  
768 Science Data*, 8(2), 325–340. <https://doi.org/10.5194/essd-8-325-2016>
- 769 Lee, K., Kim, T. W., Byrne, R. H., Millero, F. J., Feely, R. A., & Liu, Y. M. (2010). The universal  
770 ratio of boron to chlorinity for the North Pacific and North Atlantic oceans. *Geochimica et  
771 Cosmochimica Acta*, 74(6), 1801–1811. <https://doi.org/10.1016/j.gca.2009.12.027>
- 772 Lenton, A., Tilbrook, B., Law, R. M., Bakker, D., Doney, S. C., Gruber, N., et al. (2013). Sea–air  
773 CO<sub>2</sub> fluxes in the Southern Ocean for the period 1990&ndash;2009. *Biogeosciences*,  
774 10(6), 4037–4054. <https://doi.org/10.5194/bg-10-4037-2013>
- 775 Lovenduski, N. S., Gruber, N., Doney, S. C., & Lima, I. D. (2007). Enhanced CO<sub>2</sub> outgassing in  
776 the Southern Ocean from a positive phase of the Southern Annular Mode. *Global  
777 Biogeochemical Cycles*, 21(2), GB2026. <https://doi.org/10.1029/2006GB002900>
- 778 Lueker, T. J., Dickson, A. G., & Keeling, C. D. (2000). Ocean pCO<sub>2</sub> calculated from dissolved  
779 inorganic carbon, alkalinity, and equations for K<sub>1</sub> and K<sub>2</sub>: Validation based on laboratory  
780 measurements of CO<sub>2</sub> in gas and seawater at equilibrium. *Marine Chemistry*, 70(1–3), 105–  
781 119. [https://doi.org/10.1016/S0304-4203\(00\)00022-0](https://doi.org/10.1016/S0304-4203(00)00022-0)
- 782 MacGilchrist, G. A., Naveira Garabato, A. C., Brown, P. J., Jullion, L., Bacon, S., Bakker, D. C.  
783 E., et al. (2019). Reframing the carbon cycle of the subpolar Southern Ocean. *Science  
784 Advances*, 5(8), eaav6410. <https://doi.org/10.1126/sciadv.aav6410>
- 785 Martin, J. H., Knauer, G. A., Karl, D. M., & Broenkow, W. W. (1987). VERTEX: carbon cycling  
786 in the northeast Pacific. *Deep Sea Research Part A, Oceanographic Research Papers*, 34(2),  
787 267–285. [https://doi.org/10.1016/0198-0149\(87\)90086-0](https://doi.org/10.1016/0198-0149(87)90086-0)
- 788 Meier, W. N., Fetterer, F., Savoie, M., Mallory, S., Duerr, R., & Stroeve, J. (2017). NOAA/NSIDC  
789 Climate Data Record of Passive Microwave Sea Ice Concentration, Version 3, 1979–2018.  
790 Boulder, Colorado USA: NSIDC: National Snow and Ice Data Center.  
791 <https://doi.org/10.7265/N59P2ZTG>
- 792 Meredith, M., Sommerkorn, M., Cassotta, S., Derksen, C., Ekaykin, A., Hollowed, A., et al.  
793 (2019). Polar Regions. In H.-O. Pörtner, D. C. Roberts, V. Masson-Delmotte, P. Zhai, M.

- 794 Tignor, E. Poloczanska, et al. (Eds.), *IPCC Special Report on the Ocean and Cryosphere in*  
795 *a Changing Climate*.
- 796 Meredith, M. P., Naveira Garabato, A. C., Hogg, A. M., & Farneti, R. (2012). Sensitivity of the  
797 overturning circulation in the Southern Ocean to decadal changes in wind forcing. *Journal of*  
798 *Climate*, 25(1), 99–110. <https://doi.org/10.1175/2011JCLI4204.1>
- 799 Mikaloff Fletcher, S. E., Gruber, N., Jacobson, A. R., Gloor, M., Doney, S. C., Dutkiewicz, S., et  
800 al. (2007). Inverse estimates of the oceanic sources and sinks of natural CO<sub>2</sub> and the implied  
801 oceanic carbon transport. *Global Biogeochemical Cycles*, 21(1), GB1010.  
802 <https://doi.org/10.1029/2006GB002751>
- 803 Mongwe, N. P., Vichi, M., & Monteiro, P. M. S. (2018). The seasonal cycle of CO<sub>2</sub> and CO<sub>2</sub>  
804 fluxes in the Southern Ocean: diagnosing anomalies in CMIP5 Earth system models.  
805 *Biogeosciences*, 15(9), 2851–2872. <https://doi.org/10.5194/bg-15-2851-2018>
- 806 Morrison, A. K., & Hogg, A. M. (2013). On the Relationship between Southern Ocean Overturning  
807 and ACC Transport. *Journal of Physical Oceanography*, 43(1), 140–148.  
808 <https://doi.org/10.1175/JPO-D-12-057.1>
- 809 Morrison, A. K., Frölicher, T. L., & Sarmiento, J. L. (2015). Upwelling in the Southern Ocean.  
810 *Physics Today*, 68(1), 27–32. <https://doi.org/10.1063/PT.3.2654>
- 811 Olsen, A., Key, R. M., van Heuven, S., Lauvset, S. K., Velo, A., Lin, X., et al. (2016). The Global  
812 Ocean Data Analysis Project version 2 (GLODAPv2) – an internally consistent data product  
813 for the world ocean. *Earth System Science Data*, 8(2), 297–323. [https://doi.org/10.5194/essd-](https://doi.org/10.5194/essd-8-297-2016)  
814 [8-297-2016](https://doi.org/10.5194/essd-8-297-2016)
- 815 Orsi, A. H., Whitworth, T., & Nowlin, W. D. (1995). On the meridional extent and fronts of the  
816 Antarctic Circumpolar Current. *Deep-Sea Research Part I*, 42(5), 641–673.  
817 [https://doi.org/10.1016/0967-0637\(95\)00021-W](https://doi.org/10.1016/0967-0637(95)00021-W)
- 818 Orsi, A. H., Johnson, G. C., & Bullister, J. L. (1999). Circulation, mixing, and production of  
819 Antarctic Bottom Water. *Progress in Oceanography*, 43(1), 55–109.  
820 [https://doi.org/10.1016/S0079-6611\(99\)00004-X](https://doi.org/10.1016/S0079-6611(99)00004-X)
- 821 Peng, G., Meier, W. N., Scott, D. J., & Savoie, M. H. (2013). A long-term and reproducible passive  
822 microwave sea ice concentration data record for climate studies and monitoring. *Earth System*  
823 *Science Data*, 5(2), 311–318. <https://doi.org/10.5194/essd-5-311-2013>
- 824 Perez, F. F., & Fraga, F. (1987). Association constant of fluoride and hydrogen ions in seawater.  
825 *Marine Chemistry*, 21(2), 161–168. [https://doi.org/10.1016/0304-4203\(87\)90036-3](https://doi.org/10.1016/0304-4203(87)90036-3)
- 826 Prend, C. J., Gray, A. R., Talley, L. D., Gille, S. T., Haumann, F. A., Johnson, K. S., et al. (n.d.).  
827 Indo-Pacific sector dominates Southern Ocean carbon outgassing. *Submitted to Nature*  
828 *Communications*.
- 829 Le Quéré, C., Rödenbeck, C., Buitenhuis, E. T., Conway, T. J., Langenfelds, R., Gomez, A., et al.  
830 (2007). Saturation of the Southern Ocean CO<sub>2</sub> Sink due to recent climate change. *Science*,  
831 316(5832), 1735–1738. <https://doi.org/10.1126/science.1136188>
- 832 Sarmiento, J. L., & Gruber, N. (2006). *Ocean Biogeochemical Dynamics*. Princeton University  
833 Press. Princeton, NJ: Princeton University Press. Retrieved from

- 834 <http://www.up.ethz.ch/publications/books.html>
- 835 Sarmiento, J. L., Toggweiler, J. R., Najjar, R., Webb, D. J., Jenkins, W. J., Wunsch, C., et al.  
836 (1988). Ocean Carbon-Cycle Dynamics and Atmospheric pCO<sub>2</sub>. *Philosophical Transactions*  
837 *of the Royal Society A*, 325(1583), 3–21. <https://doi.org/10.1098/rsta.1988.0039>
- 838 Skinner, L. C., Fallon, S., Waelbroeck, C., Michel, E., & Barker, S. (2010). Ventilation of the deep  
839 Southern Ocean and deglacial CO<sub>2</sub> rise. *Science*, 328(May), 1147–1152.  
840 <https://doi.org/10.1126/science.1183627>
- 841 Speer, K., Rintoul, S. R., & Sloyan, B. (2000). The Diabatic Deacon Cell. *Journal of Physical*  
842 *Oceanography*, 30(12), 3212–3222. [https://doi.org/10.1175/1520-](https://doi.org/10.1175/1520-0485(2000)030<3212:TDDC>2.0.CO;2)  
843 [0485\(2000\)030<3212:TDDC>2.0.CO;2](https://doi.org/10.1175/1520-0485(2000)030<3212:TDDC>2.0.CO;2)
- 844 Takahashi, T., Sutherland, S. C., Sweeney, C., Poisson, A., Metzl, N., Tilbrook, B., et al. (2002).  
845 Global sea-air CO<sub>2</sub> flux based on climatological surface ocean pCO<sub>2</sub>, and seasonal biological  
846 and temperature effects. *Deep Sea Research Part II: Topical Studies in Oceanography*, 49(9),  
847 1601–1622. [https://doi.org/10.1016/S0967-0645\(02\)00003-6](https://doi.org/10.1016/S0967-0645(02)00003-6)
- 848 Takahashi, T., Sutherland, S. C., Wanninkhof, R., Sweeney, C., Feely, R. A., Chipman, D. W., et  
849 al. (2009). Climatological mean and decadal change in surface ocean pCO<sub>2</sub>, and net sea-air  
850 CO<sub>2</sub> flux over the global oceans. *Deep-Sea Research Part II: Topical Studies in*  
851 *Oceanography*, 56(8–10), 554–577. <https://doi.org/10.1016/j.dsr2.2008.12.009>
- 852 Talley, L. D. (2013). Closure of the global overturning circulation through the Indian, Pacific, and  
853 Southern Oceans: Schematics and transports. *Oceanography*, 26(1), 80–97.  
854 <https://doi.org/10.5670/oceanog.2013.07>
- 855 Tamsitt, V., Drake, H. F., Morrison, A. K., Talley, L. D., Dufour, C. O., Gray, A. R., et al. (2017).  
856 Spiraling pathways of global deep waters to the surface of the Southern Ocean. *Nature*  
857 *Communications*, 8(1), 1–10. <https://doi.org/10.1038/s41467-017-00197-0>
- 858 Tamsitt, V., Talley, L. D., & Mazloff, M. R. (2019). A Deep Eastern Boundary Current Carrying  
859 Indian Deep Water South of Australia. *Journal of Geophysical Research: Oceans*, 124(3),  
860 2218–2238. <https://doi.org/10.1029/2018JC014569>
- 861 Ting, Y. H., & Holzer, M. (2017). Decadal changes in Southern Ocean ventilation inferred from  
862 deconvolutions of repeat hydrographies. *Geophysical Research Letters*, 44(11), 5655–5664.  
863 <https://doi.org/10.1002/2017GL073788>
- 864 Toggweiler, J. R. (1999). Variation of atmospheric CO<sub>2</sub> by ventilation of the ocean’s deepest  
865 water. *Paleoceanography*, 14(5), 571. <https://doi.org/10.1029/1999PA900033>
- 866 Toggweiler, J. R., & Russell, J. (2008). Ocean circulation in a warming climate. *Nature*,  
867 451(7176), 286–288. <https://doi.org/10.1038/nature06590>
- 868 Toggweiler, J. R., & Samuels, B. (1995). Effect of drake passage on the global thermohaline  
869 circulation. *Deep Sea Research Part I: Oceanographic Research Papers*, 42(4), 477–500.  
870 [https://doi.org/10.1016/0967-0637\(95\)00012-U](https://doi.org/10.1016/0967-0637(95)00012-U)
- 871 Volk, T., & Hoffert, M. I. (1985). Ocean Carbon Pumps: Analysis of Relative Strengths and  
872 Efficiencies in Ocean-Driven Atmospheric CO<sub>2</sub> Changes. In E. Sundquist & W. Broecker  
873 (Eds.), *The Carbon Cycle and Atmospheric CO<sub>2</sub>: Natural Variations Archean to Present*

- 874 (Vol. 32, pp. 99–110). American Geophysical Union (AGU).  
875 <https://doi.org/10.1029/GM032P0099>
- 876 Waugh, D. W., Primeau, F., DeVries, T., & Holzer, M. (2013). Recent changes in the ventilation  
877 of the southern oceans. *Science*, 339(6119), 568–570.  
878 <https://doi.org/10.1126/science.1225411>
- 879 Williams, N. L., Juranek, L. W., Feely, R. A., Johnson, K. S., Sarmiento, J. L., Talley, L. D., et al.  
880 (2017). Calculating surface ocean pCO<sub>2</sub> from biogeochemical Argo floats equipped with pH:  
881 An uncertainty analysis. *Global Biogeochemical Cycles*, 31(3), 591–604.  
882 <https://doi.org/10.1002/2016GB005541>
- 883 Wilson, E. A., Riser, S. C., Campbell, E. C., Wong, A. P. S., Wilson, E. A., Riser, S. C., et al.  
884 (2019). Winter Upper-Ocean Stability and Ice–Ocean Feedbacks in the Sea Ice–Covered  
885 Southern Ocean. *Journal of Physical Oceanography*, 49(4), 1099–1117.  
886 <https://doi.org/10.1175/JPO-D-18-0184.1>
- 887 Wu, Y., Hain, M. P., Humphreys, M. P., Hartman, S., & Tyrrell, T. (2019). What drives the  
888 latitudinal gradient in open-ocean surface dissolved inorganic carbon concentration?  
889 *Biogeosciences*, 16(13), 2661–2681. <https://doi.org/10.5194/bg-16-2661-2019>
- 890